International Journal of Greenhouse Gas Control 126 (2023) 103909

Contents lists available at ScienceDirect

International Journal of Greenhouse Gas Control

journal homepage: www.elsevier.com/locate/ijggc

The thermal properties of set Portland cements – a literature review in the context of CO_2 injection well integrity

T.K.T. Wolterbeek [1,2,*], S.J.T. Hangx [1]

[1] Earth Simulation Lab, Department of Earth Sciences, Utrecht University, Princetonlaan 4, 3584 CB, Utrecht, The Netherlands
[2] now at Shell Global Solutions International B.V., Grasweg 31, 1031 HW, Amsterdam, The Netherlands

A B S T R A C T

Depleted hydrocarbon reservoirs are a promising target for CO_2 sequestration. Injection of cold CO_2 into such geological reservoirs will cause thermal stresses and strains in wellbore casings, cement seals and surrounding rock, which may lead to the creation of unwanted pathways for seepage. Joule-Thomson effects could potentially produce freezing conditions. The design of CO_2 injector wells must be able to cope with these thermal loads. While numerical modelling can be used to develop our understanding and assess the impact of thermal processes on wellbore integrity, such analyses require reliable input data for material properties, such as those of the cement seals. This critical review provides an overview of existing lab measurements and theoretical considerations to help constrain the thermal behaviour of Portland cement under relevant subsurface conditions. Special attention is given to the i) thermal conductivity, ii) specific heat capacity, and iii) coefficient of thermal expansion. Influences on these properties of factors such as a) temperature, b) pressure, c) mixing water-to-cement ratio, d) extent of hydration, e) porosity, and f) pore fluid saturation are discussed. Our review has shown that lab datasets obtained under relevant downhole conditions are limited, constraining the input for numerical assessment of wellbore cement integrity.

1. Introduction

Carbon Capture and Storage (CCS) is widely seen as imperative for achieving climate goals, because CCS could enable a quick reduction of CO_2 emissions related to fossil fuel use, allowing society to meet its energy demand while transitioning to sustainable energy sources (Linda and Singh, 2021; Mikunda et al., 2021; Procesi et al., 2013; Szulczewski et al., 2012). For CCS to be an effective mitigative measure, however, large volumes of CO_2 must be captured and then sequestered long-term. Injection into underground rock formations such as depleted hydrocarbon reservoirs is viewed as a technologically advanced and attractive option, since such reservoirs could provide the storage capacity required (Bachu, 2008; Belfroid et al., 2021; Godec et al., 2011; Hepple and Benson, 2005; Sanchez Fernandez et al., 2016). The success of geological sequestration will hinge on our ability to hold the CO_2 within the intended storage complex. In this context, seepage along wells is widely recognized as one of the main containment risks (Carey, 2013; Gasda et al., 2004; Schimmel et al., 2019; Wolterbeek et al., 2021b; Zhang and Bachu, 2011).

Wells are indispensable for CCS, providing entry for CO_2 injection into the reservoir situated at depth. Yet, in so doing wells also penetrate and disrupt the hydraulic seals naturally provided by caprocks overlying the storage formation, creating potential seepage pathways (Dusseault et al., 2000; Gasda et al., 2004; Kiran et al., 2017; Zhang and Bachu, 2011). Safeguarding zonal isolation integrity, i.e., preventing unsolicited flow along the wellbore trajectory, therefore is a key aspect of well design. Sealant materials must be able to withstand the pressures and temperatures at depth (Moghadam et al., 2021; Nelson and Guillot, 2006; Wolterbeek et al., 2021a), chemical conditions presented by CO_2 and resident formation fluids (Carey, 2013; Choi et al., 2013; Jahanbakhsh et al., 2021; Wolterbeek et al., 2019, 2016b, 2013; Wolterbeek and Raoof, 2018), and mechanical loads resulting from injection or other well operations, as well as tectonic forces (Bois et al., 2018, 2013; Dou et al., 2020; Gu et al., 2017; Hangx et al., 2015; Lecampion et al., 2013; Orlic, 2009; Thiercelin et al., 1997; Wolterbeek et al., 2016a). Conventional well designs rely on steel pipe and Portland cement to provide mechanical strength and hydraulic sealing. If the cement gets damaged this can impair zonal isolation integrity.

Thermal stresses and associated damage are a well-known source of failure in cement sheaths, particularly if they get subjected to thermal cycling, i.e., recurrent changes in temperature (Albawi, 2013; De Andrade et al., 2015; Heathman and Beck, 2006; Ichim and Teodoriu, 2017; Roy et al., 2018, 2016; Vrålstad et al., 2015). Being able to withstand thermal loads is especially relevant for CCS injection wells, because the CO_2 will usually be much colder than the downhole environment into which it is injected. For efficiency, captured CO_2 is

* Corresponding author
E-mail address: Tim.Wolterbeek@shell.com (T.K.T. Wolterbeek).

https://doi.org/10.1016/j.ijggc.2023.103909
Received 6 December 2022; Received in revised form 1 May 2023; Accepted 9 May 2023
Available online 24 May 2023
1750-5836/© 2023 The Author(s). Published by Elsevier Ltd. This is an open access article under the CC BY license (http://creativecommons.org/licenses/by/4.0/).

preferentially transported in dense phase. This involves pressures of >7 MPa, while supply temperatures typically range 2-10°C and 15-25°C for offshore and onshore pipeline transport, respectively (Acevedo and Chopra, 2017; Lindeberg, 2011). By contrast, most subsurface formations are much warmer (e.g., the initial storage temperature at the Snøhvit CCS project site was 95°C at 2.6 km depth – Hansen et al., 2013; Ringrose, 2020). In general, potential reservoirs situated at 2-5 km depth will have temperatures of 60-150°C, assuming a typical geothermal gradient of 30°C km^{-1}. Given this large temperature contrast, steady-state CO_2 injection will invariably result in progressive cooldown of the near-wellbore region. Conversely, interruptions of injection (e.g., during well servicing or shut-ins) may allow the well temperature to rise again, as heat gets supplied from rock in the wider surroundings.

Additional thermal effects are expected for CO_2 storage into depleted hydrocarbon reservoirs (Hamza et al., 2021; Hoteit et al., 2019). Residual pressures after production are typically subhydrostatic and often substantially lower than the intended CO_2 supply pressure during subsequent CCS activities (Samuel and Mahgerefteh, 2019). Under such low-pressure reservoir conditions, unimpeded inflow down the well could result in rapid, quasi-adiabatic expansion of the CO_2 into its vapor phase, with associated Joule-Thomson (J-T) effects that may produce large temperature drops along the wellbore (Acevedo and Chopra, 2017; Mathias et al., 2010; Moradi et al., 2020; Oldenburg, 2007). Theoretically, very low temperatures can be reached: cooling down to –78.5°C for isenthalpic expansion to atmospheric pressure (McCollom, 2011). For injection into ultra-depleted formations with residual pressures of only 1-2 MPa, temperatures down to –20°C are not inconceivable. Careful CCS injection well design can help avoid excessive J-T effects during normal operations, e.g., by installing slimmer tubing that creates sufficient backpressure to prevent CO_2 from reaching vapor phase conditions inside the well (so-called "reverse velocity string" techniques; Acevedo and Chopra, 2017). Nevertheless, in the highly unlikely event of a CO_2 blowout, the casings and cement may get subjected to significant cooling and possibly even freezing conditions. In case of a large pressure drop persisting over a prolonged period of time, even small leaks may locally induce considerable J-T cooling.

These changes in well temperature can result in thermal strains and associated stresses in the steel casings, cement sheaths, and surrounding rock formations (Bois et al., 2018, 2013; Roy et al., 2018). Strong thermal contraction of the casing upon cooling may induce debonding and create microannuli along the cement interface (Dou et al., 2020; Huan et al., 2021; Moghadam et al., 2021; Roy et al., 2018). Repeated temperature variations due to intermittent injection could lead to fatigue and reduced fracture-resistance of the cement sheaths (Heathman and Beck, 2006; Nygaard et al., 2014). Numerical models are developed to better understand and assess the impact of such processes on zonal isolation integrity (Asamoto et al., 2013; Nygaard et al., 2014; Roy et al., 2018). However, while critical input for such modelling analyses, the thermal properties of Portland-based wellbore cements remain challenging to constrain, with only sparse and scattered experimental data available, especially for the elevated pressures expected downhole.

This study provides a critical review of available lab measurements and theoretical considerations, to help constrain the thermal properties of Portland cement for numerical modelling of wellbore behaviour under specific CO_2 injection scenarios. Reviewed cement properties include the i) thermal conductivity, ii) specific heat capacity, and iii) coefficient of thermal expansion. We will show that the test conditions during measurement must be considered carefully to determine whether cement lab data are representative for downhole behaviour and hence suitable for numerical analysis of wellbore integrity or not.

2. Scope and limitations of this review

The mechanical, thermal, and transport properties of set wellbore cement are key input parameters for quantitative analysis of zonal isolation integrity. The results of numerical simulations are usually found to depend strongly on the properties and material models assumed for the cement seals (Dou et al., 2020; Lecampion et al., 2011; Nygaard et al., 2014; ter Heege et al., 2015; Wise et al., 2020). In this context, this review aims to define relevant parameter ranges for the thermal properties. Our primary focus will be on API Class G and H cement, which are nowadays by far the most commonly used in well cementing (Nelson and Guillot, 2006; Nelson and Michaux, 2006). Given their relevance for older wells, further distinctions between (legacy) types of oil well cement will be made insofar as possible on the basis of existing data (Table 1). To help constrain cement behaviour under specific downhole conditions, the influences of factors such as i) temperature, ii) pressure, iii) mixing water-to-cement mass (w:c) ratio, iv) extent of hydration, v) porosity, and vi) degree of pore fluid saturation will be discussed in some detail. Given the plethora of different cementing additives, extenders, and fillers in current or historic use, however, it is impractical and therefore beyond the scope of this review to comprehensively cover effects of admixtures on the thermal properties of wellbore cement. While additives are touched upon in specific cases, the discussions below will be largely restricted to the behaviour of neat cement pastes.

3. Thermal conductivity

3.1. Basic definitions

Thermal conduction is the process of energy transfer between hotter and colder regions of a material due to vibrations and collisions of its constituent particles (e.g., atoms, free electrons). Heat transfer in set wellbore cement occurs primarily through thermal conduction, possibly aided by minor thermal expansion-driven advection of the capillary pore fluid phase (Section 5). Nevertheless, the rate of flow of heat in cement can usually be described in terms of Fourier's law:

$$\mathbf{q} = -\boldsymbol{\lambda}\nabla T \tag{1}$$

Here, $\mathbf{q}$ [W m^{-2}] denotes the heat flux, ∇T [K m^{-1}] is the temperature gradient, and $\boldsymbol{\lambda}$ [W m^{-1} K^{-1}] is the thermal conductivity of the cement. Note $\boldsymbol{\lambda}$ can be anisotropic and may vary with temperature and other environmental parameters. In absence of internal heat sources (e.g., after cessation of hydration reactions), the rate of change in temperature, $\partial T/\partial t$ [K s^{-1}], will be proportional to the rate of change in internal heat energy per unit volume of cement, $\partial Q/\partial t$ [W m^{-3} s^{-1}] (Carslaw and

Table 1
Overview of the main types of Portland-based wellbore cements

classification		typical anhydrous composition [wt.%]				nominal w:c [-]
API	ASTM	C3S (alite)	C2S (belite)	C3A	C4AF	
Class A	CEM I	45	27	11	8	0.46
Class B	CEM II	44	31	5	13	0.46
Class C	CEM III	53	19	11	9	0.56
Class D		28	49	4	12	0.38
Class E		38	43	4	9	0.38
Class G*	Nominal II	50	30	5	12	0.44
Class H*	Nominal II	50	30	5	12	0.38

Typical anhydrous compositions and nominal mixing water-to-cement mass ratios (w:c) for API classified cements. Data obtained from Nelson and Michaux (2006). For the calculations performed in CemGEMS (Section 4.3.1), listed compositions were renormalized to yield C3S + C2S + C3A + C4AF = 100%. Composition is indicated using cement chemistry notation, where C = CaO, S = SiO_2, A = Al_2O_3, F = Fe_2O_3 (Taylor, 1992). *For Class G and H cement, API recognizes 'moderate' and 'high' sulphate-resistant grades (denoted MSR and HSR, respectively – API Specification 10A/ISO 10426-1). Nominally, MSR grades correspond with ASTM Type II cement, whereas HSR grades can approach ASTM Type V cement compositions.

Jaeger, 1947):

$$\frac{\partial Q}{\partial t} = \rho c_p \frac{\partial T}{\partial t} \tag{2}$$

Here, ρ [kg m^{-3}] and c_p [J kg^{-1} K^{-1}] are the density and specific heat capacity (Section 4), respectively. Now considering flow of heat into and out of a small reference volume of cement, application of conservation of energy yields (Carslaw and Jaeger, 1947):

$$\rho c_p \frac{\partial T}{\partial t} + \nabla \cdot \mathbf{q} = 0 \tag{3}$$

Here, $\nabla \cdot \mathbf{q}$ [W m^{-3}] is the divergence of the heat flux. For a homogeneous, isotropic solid having a thermal conductivity independent of temperature, Equation 3 can be simplified to (Carslaw and Jaeger, 1947):

$$\frac{\partial T}{\partial t} = \frac{\lambda}{\rho c_p} \nabla \cdot \nabla T = a \nabla^2 T \tag{4}$$

Here, λ [W m^{-1} K^{-1}] is the isotropic thermal conductivity, $\nabla^2 T$ [K m^{-2}] is the Laplacian of the temperature (or, equivalently, the divergence of the temperature gradient) and a [m^2 s^{-1}] is the thermal diffusivity. In the reviewed literature, cement heat transfer properties are variably reported in terms of either thermal conductivity or thermal diffusivity.

3.2. Experimental thermal conductivity data available in the literature

Various lab techniques are employed to measure the thermal conductivity (λ) of cements (Asadi et al., 2018), including steady state and transient plane source methods (Baghban et al., 2013; Bentz, 2007; He, 2005; Cuello Jimenez et al., 2017; Log and Gustafsson, 1995), line source heater methods (García et al., 1989; Kim and Oh, 2019), and laser flash methods (Xu and Chung, 2000a, 2000b). While different in detailed analysis and sample geometry, most lab methods have in common that they involve the imposition of some temperature difference across a cement sample, followed by monitoring of its response (either in terms of temperature evolution or heat flow) to derive the thermal properties. It should be noted that such heating can cause significant loss of evaporable water from the cement sample, especially in measurements at higher temperature, because the experiments are typically conducted at ambient pressure and room humidity (Cuello Jimenez et al., 2017). Though seemingly common in lab tests, such strong drying effects are unlikely to occur under downhole conditions.

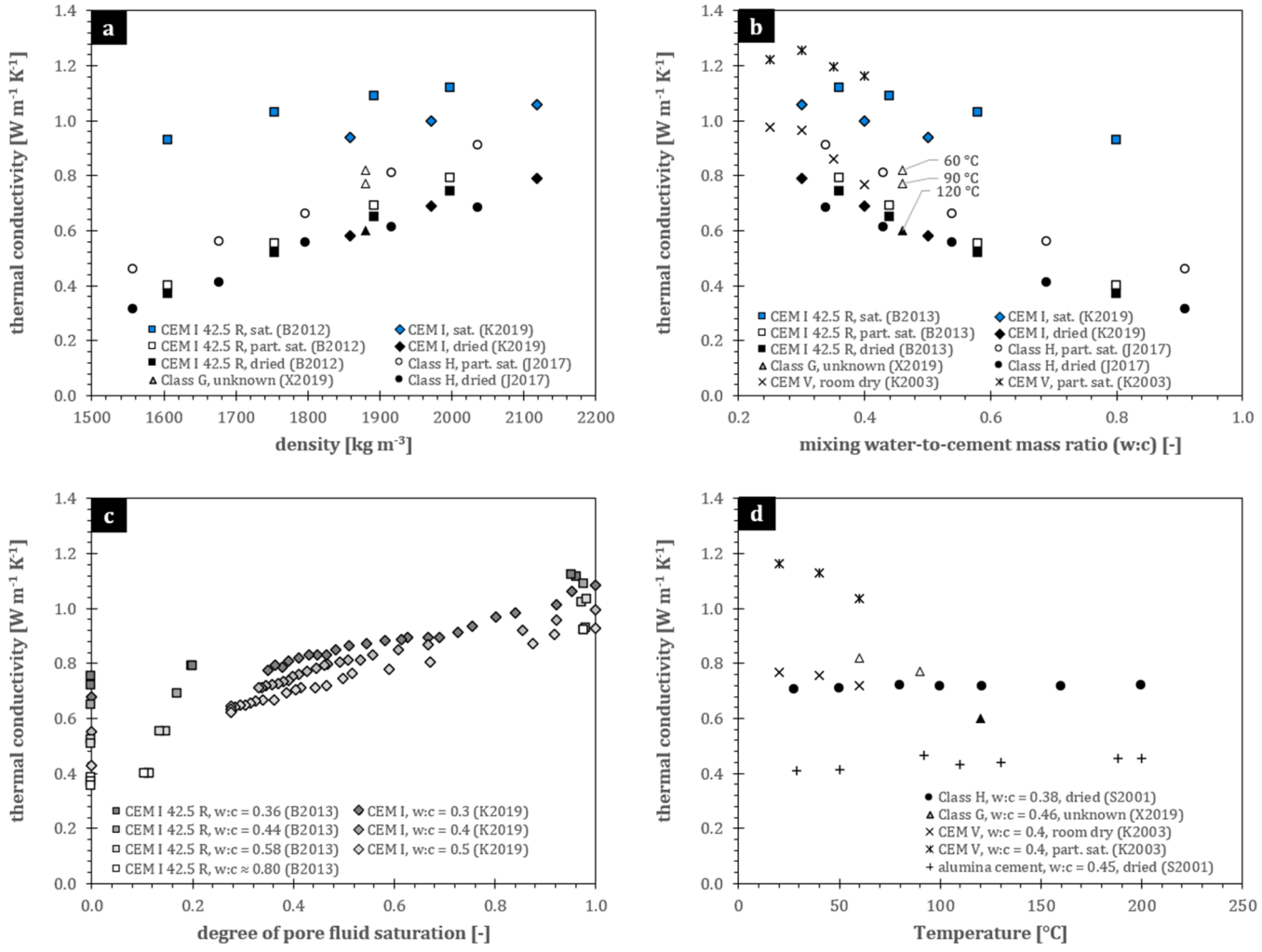

Figure 1. Selected thermal conductivity data for different classes of neat cement, plotted as function of a) density, b) water-to-cement mass ratio, c) degree of pore fluid saturation and d) temperature. Data include ASTM CEM I 42.5 R cement (squares – Baghban et al., 2013) and ASTM CEM I cement (diamonds – Kim and Oh, 2019; Kim et al., 2017), both of which may be regarded as proxies for API Class A cement (Table 1), as well as API Class G cement (triangles – Song et al., 2019), and API Class H cement (circles – Cuello Jimenez et al., 2017; Santoyo et al., 2001). Also plotted are data for ASTM Type V cement (crosses – Kim et al., 2003). Note that in some studies the highest water-to-cement ratio slurries were stabilized using viscosifier additives. For most data, the degree of pore fluid saturation was unconstrained during measurement (data plotted in white in Figures 1a, 1b and 1d) or the samples were dried prior to testing (black data in Figures 1a, 1b and 1d). Under downhole pressure, the porosity is likely saturated with aqueous fluid (limited available data for confirmed water-saturated samples is plotted in blue).

At the elevated pressures encountered at depth, water present in the cement capillary porosity will not evaporate but remain in a liquid state upon heating. Unfortunately, very few studies have considered the degree of pore fluid saturation in their samples, whereas many of the reviewed lab datasets appear to include notable drying-out effects (Figure 1). Experimentally obtained λ for wellbore cement should therefore be considered with caution. This is especially important for assessing the impact of downhole temperature on cement thermal conductivity, as will be highlighted below.

3.2.1. Effect of cement pore fluid saturation

Figure 1a-d shows λ for different neat cements as a function of density, mixing water-to-cement mass (w:c) ratio, degree of pore fluid saturation, and temperature, respectively. The data include ASTM CEM I 42.5 R cement at 23°C (squares – Baghban et al., 2013), ASTM CEM I cement at 22°C (diamonds – Kim and Oh, 2019; Kim et al., 2017), ASTM Type V cement at 20-60°C (crosses – Kim et al., 2003), API Class H cement at 40 to 83°C (circles – Cuello Jimenez et al., 2017; Santoyo et al., 2001), and API Class G cement at 60 to 120°C (triangles – Song et al., 2019). Though not specified in the publications explicitly, it seems reasonable to assume all data were collected at ambient pressure. Only a few studies provide quantitative constraints on the degree of pore fluid saturation in their samples (Baghban et al., 2013; Kim and Oh, 2019; Kim et al., 2017). In Figure 1a-b, data plotted in blue correspond to (nearly) water-saturated cement (93.8-98.2% saturated; Baghban et al., 2013), while data plotted in black represent samples that were first dried to constant mass at 105°C (Baghban et al., 2013; Kim et al., 2017), a procedure in which virtually all evaporable water is removed (Taylor, 1992). A third set of samples with intermediate saturations is plotted in white (10.4-21.7% saturated; Baghban et al., 2013). Figure 1c shows λ as a function of pore fluid saturation degree for CEM I cement (w:c-ratio indicated in grey scale). Because of the stark contrast between the thermal conductivities of water (0.6 W m^{-1} K^{-1} at 20°C, 0.1 MPa) and air (0.025 W m^{-1} K^{-1} at 20°C, 0.1 MPa), any loss of pore fluid saturation (e.g., samples drying out) has a profound impact on λ. In general, the effective thermal conductivity of cementitious materials diminishes markedly with decreasing moisture content (Figure 1c; Asadi et al., 2018; Mnahoncakova et al., 2006). Note that cement presumably remains close to saturated under the pressures encountered downhole (Badino, 2010), rendering the λ obtained for dried cement samples inappropriate for bulk cement behaviour under typical wellbore conditions.

3.2.2. Effects of cement type and mixing water-to-cement mass ratio

Note ASTM CEM I cements are considered equivalent to API Class A cement (Table 1), presumably rendering the λ values representative as well (Figure 1). Cuello Jimenez et al. (2017) provide λ for Class H cement at 40 to 83°C. Their samples were either oven dried at 65.6°C or left "wetted", but pore fluid saturation was not controlled, nor monitored, and partial drying is likely (W. Cuello Jimenez, pers. comm., April 2023). Assuming dried and partially saturated conditions for the two sets of samples, respectively, they are correspondingly plotted in black and white (circles, Figure 1a-b). Similarly, Song et al. (2019) provide λ-data for API Class G cement (triangles, Figure 1). Kim et al. (2003) report λ for "wet" and "dried" samples of ASTM Type V cement (similar to HSR grades of Class G and H cement) as function of w:c ratio (Figure 1b, showing data for 20°C) and temperature (Figure 1d, showing data for w:c ratio = 0.4). Kim et al. (2003) also performed a reference experiment on "wet" ASTM CEM I cement (w:c ratio = 0.4), yielding a λ of 1.15 W m^{-1} K^{-1} at 20°C, which is close to the values they obtained for ASTM CEM V cement under the same conditions (1.16 W m^{-1} K^{-1}). Yoon et al. (2014) report a relatively high λ of 1.28 W m^{-1} K^{-1} at 20°C for ASTM CEM III cement mixed at a w:c ratio of 0.4 and cured in water for 28 days.

Based on the data in Figure 1, the following overall trends can be observed: i) the thermal conductivity of water-saturated CEM I cement (on the order of ~1 W m^{-1} K^{-1}) is approximately double that of dried CEM I cement at 23°C, ii) for all classes of cement, the thermal conductivity increases with increasing density or, equivalently, decreasing mixing water-to-cement mass (w:c) ratio, iii) for dried samples, different types of cement generally show roughly similar λ (e.g., see alignment of black data points in Figure 1b), though CEM III and V cements may have relatively higher conductivity based on limited data. Overall, it should be noted that the impact of degree of pore fluid saturation on λ tends to exceed effects due to cement type or mixing w:c-ratios over the ranges investigated.

3.2.3. Variation with temperature in experiments

A limited number of studies has considered the temperature dependence of cement thermal conductivity. Santoyo et al. (2001) measured the λ of neat API Class H cement (w:c = 0.38) and five other cement formulations as a function of temperature over the range 28–200°C, without confirming the pore fluid saturation. They found that the thermal conductivity of API Class H cement (presumably dried samples) remained essentially constant with temperature (Figure 1d). Cuello Jimenez et al. (2017) conducted tests on API Class H cement at temperatures of 40 to 83°C, but reported only averaged values for λ over this range. Song et al. (2019) reported measurements on API Class G cement at 60°C, 90°C and 120°C (triangles – Figure 1), where they observed a decrease in λ from 0.82 to 0.60 W m^{-1} K^{-1} with increasing temperature. However, whether this effect is representative for Class G cement under downhole pressures and saturation degrees is questionable. Since Song et al. (2019) performed measurements at ambient pressure and room humidity, the observed decrease in λ with increasing temperature might also be explained wholly in terms of loss of evaporable porewater from the cement matrix. The saturation state of the 60°C and 90°C samples is difficult to constrain (hence plotted in white in Figure 1), but it is not unreasonable to assume that the 120°C sample suffered significant drying effects, since 120°C exceeds both the boiling point of water at ambient pressure and commonly employed sample drying-technique temperatures (e.g., 105°C; Taylor, 1992). Note that the λ at 120°C indeed agrees well with the main trends seen for oven-dried cement samples (black triangle – Figure 1b), while the gradual decrease from 60°C to 120°C could be interpreted as a result of progressive porewater loss (compare Figures 1b and 1d). Kim et al. (2003) reported experiments on ASTM Type V cement at 20-60°C (Figure 1d). Their "dry" samples also show little change with temperature, while their "wet" samples show a modest decrease like that observed by Song et al. (2019). Principally, it should be possible to avoid drying effects and porewater loss by pressurizing the samples during measurement. Unfortunately, the authors were unable to find any experimental data obtained at elevated pressure in their survey of the literature. Based on dried cement data alone, the variation in λ with temperature is expected to be minor. However, note that the hydrated cement chemistry changes significantly with temperature, which will potentially cause discontinuities, e.g., above 110°C (Section 5.3.4).

3.3. Model estimations of thermal conductivity

While the thermal conductivity of wellbore cement is traditionally determined experimentally (Nelson and Guillot, 2006), developments in numerical methods and model-based evaluation of the thermal conductivity of cementitious materials provide potentially interesting alternatives. Specifically, advances in molecular-dynamics simulation of the atomic structure of some major constituents of Portland cement, such as jennite and tobermorite-based structural endmembers for the calcium silicate hydrate (C-S-H) gel phase, enabled first-principles computation of their microscale properties (Fan and Yang, 2018; Hong et al., 2020; Qomi et al., 2015; Sarkar and Mitra, 2021). Upscaling to macroscopic thermal properties of cement paste is subsequently achieved using composite models and mean-field homogenization theory, such as the Mori-Tanaka scheme (Qomi et al., 2015; Sarkar and

Mitra, 2021). Other formulations include parallel and series models, Hashin-Shtrikman bounds (Baghban et al., 2018, 2013; Hashin and Shtrikman, 1962), Reuss-Voight-Hill average-based models (Breuer et al., 2020), Russell and Frey models, and coherent potential models (see Hong et al., 2020 for a comparative analysis of mixing models).

3.3.1. Effect of porosity

Sarkar and Mitra (2021) provide estimates for the effective mean (volumetric) thermal conductivity of jennite (1.007 W m^{-1} K^{-1}) and various forms of tobermorite (1.470-4.510 W m^{-1} K^{-1}) based on molecular-dynamics simulations. Similarly, Hong et al. (2020) report 1.141 ± 0.026 W m^{-1} K^{-1} for jennite, and Qomi et al. (2015) report values of 0.98 ± 0.2 W m^{-1} K^{-1} for jennite and tobermorite, and 1.32 ± 0.2 W m^{-1} K^{-1} for portlandite. Based on jennite and tobermorite data, Sarkar and Mitra (2021) further calculate thermal conductivities for high- and low-density forms of nanoporous C-S-H gel, yielding λ of 1.311 W m^{-1} K^{-1} and 0.988 W m^{-1} K^{-1}, respectively. Taking an average composition with 29% nanoporosity, they report 1.177 W m^{-1} K^{-1} as typical λ for the C-S-H gel phase in Portland-based cements and additionally provide estimates for cements that also contain macroporosity (Sarkar and Mitra, 2021). It matters significantly whether these macropores contains water or air. For cement with water-filled macroporosities of 2.3%, 7.56% and 16.5% (i.e., total porosities of 30.7% to 40.8%, including the C-S-H gel nanoporosity), Sarkar and Mitra (2021) calculate λ of 1.161 W m^{-1} K^{-1}, 1.125 W m^{-1} K^{-1} and 1.065 W m^{-1} K^{-1}, respectively. These results show fair agreement with experimental data for water saturated cement (Figure 2). Yet, linear least squares extrapolation of the model data towards 100% porosity (grey dashed line) suggests that a typographical error in Table 5 of Sarkar and Mitra (2021), where the λ of water is listed as 0.519 W m^{-1} K^{-1} instead of 0.591 W m^{-1} K^{-1}, also affected their calculations. Taking into account this issue, a linear approximation of the form λ [W m^{-1} K^{-1}] = 1.4 − 0.8φ (black dashed line), where φ [-] is the total porosity, seems to cover both the experimental and Sarkar and Mitra-model data reasonably well. Conversely, the C-S-H paste model of Qomi et al. (2015; dotted line in Figure 2) substantially underestimates λ compared to available experimental data. Also plotted are λ-values for water saturated porous jennite (Hong et al., 2020; solid line in Figure 2). Since the other constituents of hydrated Portland cement, such as tobermorite and portlandite, tend to have higher thermal conductivities (Breuer et al., 2020; Qomi et al., 2015; Sarkar and Mitra, 2021), this jennite model could perhaps serve as lower-bound estimate for water saturated neat Portland-based wellbore cements (Figure 2).

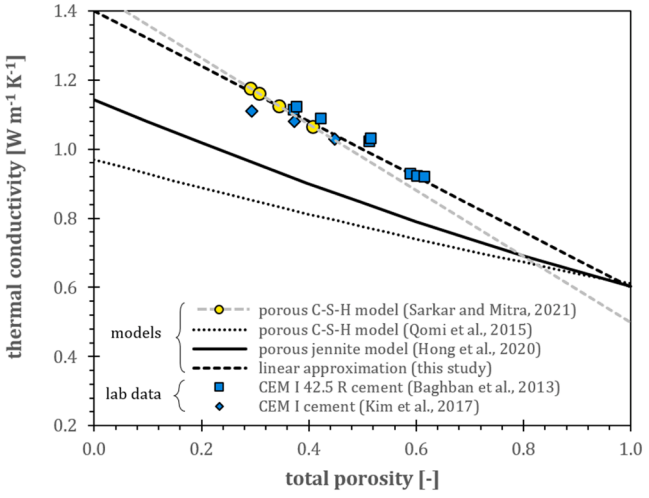

Figure 2. Thermal conductivity of water saturated cement as a function of total porosity (i.e., the sum of gel/nano-, meso-, and capillary/macro-porosity). Data include experimental λ for ASTM CEM I cement at room temperature (Baghban et al., 2013; Kim et al., 2017) and calculated λ based on molecular dynamics simulation and mean-field homogenization theory for C-S-H pastes (Qomi et al., 2015; Sarkar and Mitra, 2021) and porous jennite (Hong et al., 2020).

3.3.2. Temperature dependence in models

Recalling the challenge of evaluating how λ varies with temperature in experiments (Section 3.2.3), let us now consider some single-phase measurements and composite modelling results pertaining to temperature dependence. Figure 3 shows the thermal conductivity of water at various pressures (Lemmon et al., 2021) and λ for a number of cement constituent phases, namely portlandite (Breuer et al., 2020) and jennite (Hong et al., 2020). Over the range –30°C to 30°C, the thermal conductivity of jennite decreases slightly with increasing temperature, from 1.18 W m^{-1} K^{-1} to 1.14 W m^{-1} K^{-1}, while from 30°C to 300°C λ increases to ~1.24 W m^{-1} K^{-1}. Depending on pressure, the thermal conductivity of water tends to increase with increasing temperature over the range 0°C to 120–170°C (Lemmon et al., 2021), though it should be noted that the properties of cement pore fluid may differ significantly from bulk liquid water due to the nanoscale confining environment provided by C-S-H gel porosity (Qomi et al., 2015; Valenza II and Scherer, 2005). Nevertheless, cement thermal conductivity calculations based on jennite-tobermorite structural models, like those of Sarkar and Mitra (2021) or Hong et al. (2020), predict fairly stable to slightly increasing cement λ-values with increasing temperature. By contrast, Breuer et al. (2020) found that the thermal conductivity of portlandite [$Ca(OH)_2$] decreases with increasing temperature in lab experiments on synthetic single crystals. Since portlandite is a relatively minor phase and given the large spread in available data (for example, Qomi et al. (2015) calculated an λ of only 1.32 ± 0.2 W m^{-1} K^{-1} at room temperature), it is difficult to assess the impact of portlandite on the overall cement thermal conductivity.

3.4. Impact of cementing additives

While providing a comprehensive overview on the effects of cementing additives is beyond the scope of this review, it is interesting to note that the thermal conductivity of wellbore cement can be augmented in the slurry stage. Depending on what is desired of the set cement, one can introduce insulating or conductive additive materials. Most research in this direction to date has been focused on cement

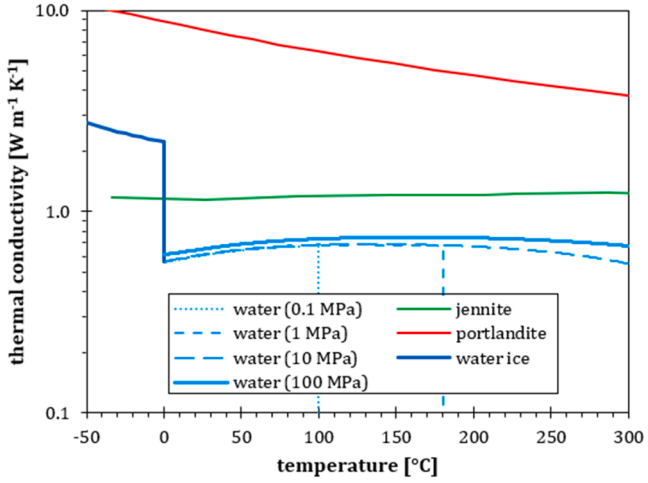

Figure 3. Thermal conductivity as function of temperature for water and two key constituents of Portland cement. Data for jennite is based on molecular-dynamics simulations, plotting λ of the non-porous structure (Hong et al., 2020). Data for portlandite is obtained in lab measurements on synthetic single crystals, plotting the Voigt-Reuss-Hill average of thermal conductivity in orthogonal crystallographic directions (Breuer et al., 2020). Data for water and water ice are from the NIST Standard Reference Database 69 (Lemmon et al., 2021) and Engineering Toolbox (2004), respectively.

formulations for geothermal energy production wells. Song et al. (2019) showed that the addition of conductive materials like graphite, iron, or copper powder (5-20% bwoc) can increase cement thermal conductivity (though an associated increase in the hardened cement porosity was found to decrease the effectiveness of adding high concentrations of graphite). Similarly, Wang et al. (2020) modified the thermal conductivity of cement by adding natural graphic flakes. They reported increases in the λ of dried samples of up to 156% but noted that these samples also showed reduced compressive strength. Cuello Jimenez et al. (2017) found that adding 20% bwoc of insulating elastomer particles (having a λ of ~0.23 W m^{-1} K^{-1}) can lower the effective thermal conductivity of wellbore cement, particularly in cement systems of higher overall density. Santoyo et al. (2001) considered the thermal conductivity of Class H cement containing silica flour, expanded perlite, and bentonite. Xu and Chung (2000a) created cement pastes with a high thermal conductivity and specific heat capacity using silane. As with the λ measurements on plain cement, note many datasets on additive-enhanced cements include unrepresentative effects due to drying of lab samples. Asadi et al. (2018) provide a recent review on the effects of additives and aggregate phases on the thermal conductivity of mortars and concrete.

4. Specific heat capacity

4.1. Basic definitions

The specific heat capacity of a material, c [J kg^{-1} K^{-1}], is a measure for the amount of heat energy that needs to be supplied to a unit mass of the material to achieve a unit increase in its temperature:

$$c = \frac{1}{\rho}\frac{\partial Q}{\partial T} \tag{5}$$

Here, Q [J m^{-3}] is the internal heat energy per unit volume, ρ [kg m^{-3}] is the density and T [K] is the temperature. Note the specific heat capacity can vary substantially with pressure and temperature, such that $c = c(p, T)$. Aside from raising its temperature, supplying heat to a material usually also causes an increase in its volume or stress state, depending on the boundary conditions under which heat is supplied. The specific heat capacity at constant pressure, $c_p(p, T)$ [J kg^{-1} K^{-1}], is usually higher than that at constant volume, $c_V(p,T)$ [J kg^{-1} K^{-1}], because at constant pressure part of the supplied heat is used to perform work (i.e., increase volume through thermal expansion), rather than raise the temperature of the material further. This difference between c_p and c_V, often expressed as the heat capacity ratio, $\gamma = c_p/c_V$ [-], is quite notable in gasses, but generally much less so in solids like cement. Nevertheless, it can be a useful distinction, relating the volumetric coefficient of thermal expansion (α_V [K^{-1}], Section 5) and isothermal bulk modulus (K [Pa]) via (e.g., Qomi et al., 2015):

$$c_p - c_V = \frac{TK\alpha_V^2}{\rho} \tag{6}$$

4.2. Experimental specific heat capacity data available in the literature

Lab methods used for measuring the specific heat capacity of cements are generally similar to traditional calorimetry techniques. For example, the specific heat capacity can be determined from the temperature rise in a calorimeter measured in response to a prescribed energy input. If the temperature response of the empty calorimeter is known (e.g., by performing a reference measurement), the specific heat capacity of a cement sample can be derived as follows (e.g., De Schutter and Taerwe, 1995):

$$c = \frac{1}{m_s}\left(\frac{E_s}{\Delta T_s} - \frac{E_r}{\Delta T_r}\right) \tag{7}$$

Here, c [J kg^{-1} K^{-1}] is the specific heat capacity of the cement, m_s [kg] is the mass of the sample, E_s and E_r [J] are the amounts of energy supplied during the sample measurement and the reference test without sample, respectively, while ΔT_s and ΔT_r [K] are the corresponding temperature changes recorded. Measurement requires the calorimeter is well-insulated and has a low thermal mass, in order to minimize heat loss (Bentz, 2007; De Schutter and Taerwe, 1995). In such tests, energy input is usually achieved by supplying a current over a known electrical resistance. For experiments on early-age cement pastes, the impact of exothermic hydration reactions occurring during measurement should be considered, e.g., by adjusting measured step changes in temperature via back-extrapolation of longer-term trends (De Schutter and Taerwe, 1995). Alternatively, lab testing could involve non-steady state heat flow measurements (Yoon et al., 2014) or measurement of differences in the amounts of heat required to increase the temperature of a sample and a known reference, such as in differential scanning calorimetry techniques. Note data obtained using methods in which the cement samples are allowed to gain or lose water during measurement may suffer significant energetic contributions from evaporation or condensation of porewater.

For practical reasons, experiments are usually performed at constant pressure, where the sample is allowed to expand or contract freely during measurement (i.e., $c = c_p$ in Equation 7). All experiments reviewed here were performed at atmospheric pressure. As with thermal conductivity data (Section 3.2), measurements of cement specific heat capacity should be considered carefully. Aside from uncertainty in how much porewater is present in the cement, heat capacity measurements may be affected by phase changes in the pore fluid (i.e., heat of evaporation or condensation) occurring as temperature is varied in the experiments. Rather than RH alone, ideally the water content of the cement should be quantified throughout measurement to account for drying and experimental artefacts. We were unable to locate data pertaining directly to API classified Portland cement formulations, but the trends for ASTM cements discussed below are considered representative.

4.2.1. Effect of degree of hydration

The specific heat capacity of neat cement ranges from about 900 to 2000 J kg^{-1} K^{-1}, depending on moisture content, and c_p generally decreases with progressive hydration, i.e., as the cement sets (Figure 4a). This decrease with extent of hydration is usually interpreted in terms of a conversion of free liquid water, which has a relatively high c_p (4186 J kg^{-1} K^{-1} at 23°C), into porewater that is chemically and physically bound within the C-S-H gel structure (Bentz, 2007; De Schutter and Taerwe, 1995). Bentz (2007) qualitatively compares the heat capacity of this porewater phase with that of water ice, noting the unusually high specific heat capacity of bulk liquid water can be attributed to energy consumed in bending and breaking of mobile hydrogen bonds. In molecular-dynamics simulations, Qomi et al. (2015) indeed showed that the confining environment provided by the C-S-H gel phase nanoporosity decreases the apparent heat capacity of water by a factor of four. In experiments, the specific heat capacity of a fully hydrated, saturated cement can be up to 20% lower than that of its fresh paste counterpart (De Schutter and Taerwe, 1995). In the field, such effects will occur largely in the first days to weeks after placement. Bentz (2007) showed that chemical shrinkage and self-desiccation during hydration of sealed cement samples produce a more pronounced decrease in c_p compared to hydration under water-saturated conditions (Figure 4a). Measurements on dried and re-saturated cement samples suggest this additional decrease may be (partially) recovered (Kim and Oh, 2019). Over longer timescales at downhole pressure, most wellbore cements will probably remain water-saturated or eventually get re-saturated after set.

4.2.2. Effects of pore fluid saturation and mixing water-to-cement ratio

Moisture content has a profound impact on the thermal properties of cementitious materials (Kim and Oh, 2019; Kim et al., 2017). The

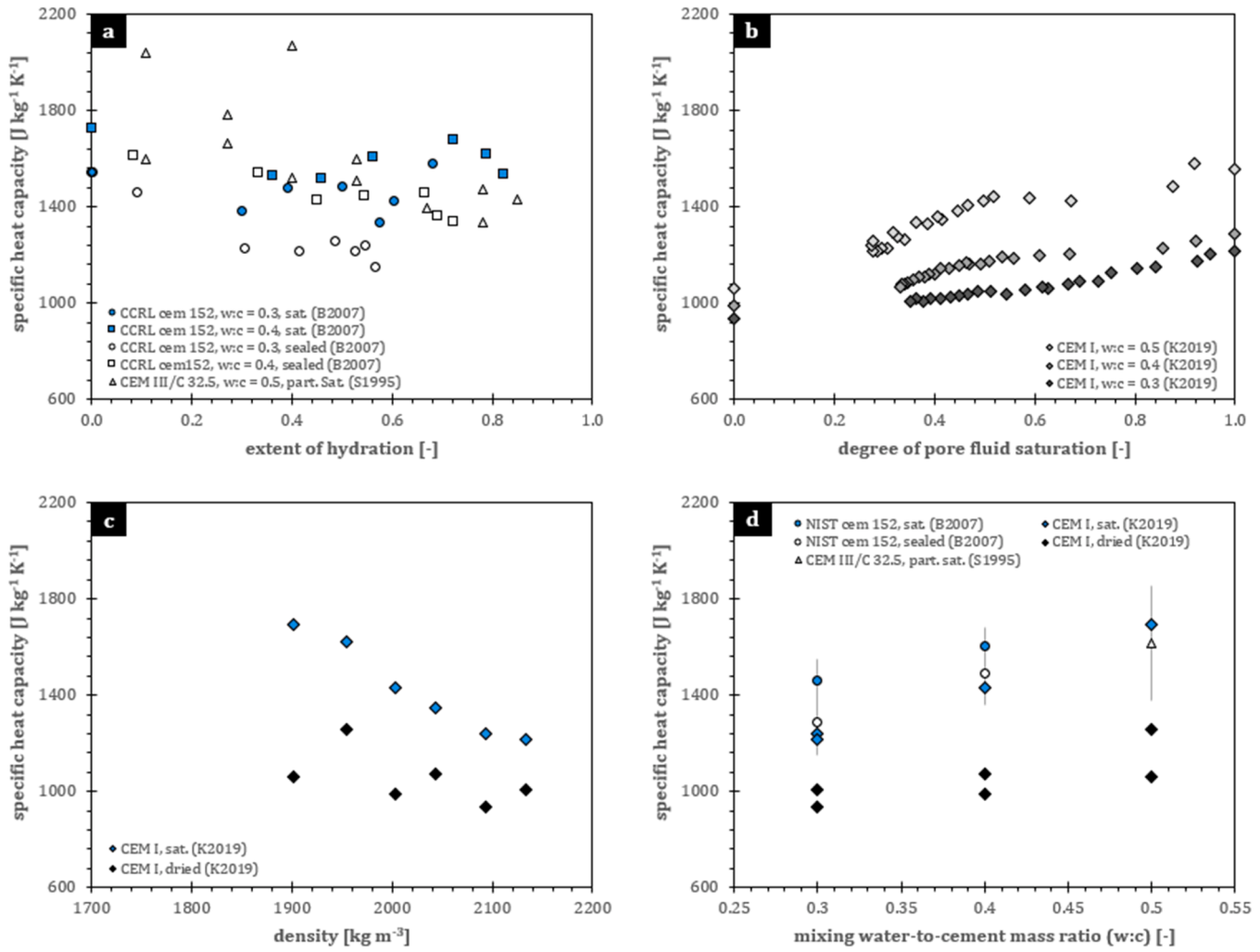

Figure 4. Selected specific heat capacity data for different classes of neat cement, plotted as a function of a) extent of hydration, b) degree of pore fluid saturation, c) density and d) mixing water-to-cement mass ratio (w:c). Plotted data include ASTM CEM I cement (diamonds – Kim and Oh, 2019; Kim et al., 2017), ASTM CEM III/C 32.5 cement (triangles – De Schutter and Taerwe, 1995) and NIST CCRL cement proficiency sample 152 (squares and circles – Bentz, 2007). Data plotted in blue pertain to water-saturated samples, while data in black represent dried cement. Samples of unknown saturation are plotted in white. In Figure 4b, grey scale indicates mixing water-to-cement mass ratio. In Figure 4d, the error bars indicate variation with extent of hydration (as shown in Figure 4a) for CCRL 152 and CEM III/C 32.5 cement.

specific heat capacity of neat cement pastes tends to increase linearly with increasing degree of pore fluid saturation (Figure 4b). Compared to their fully saturated counterpart samples, dried cement shows 15-38% lower c_p-values, where this difference is largest for lower density, higher porosity slurries (Figure 4c-d). For neat ASTM CEM I cement (equivalent to API Class A cement, Table 1), the c_p of water-saturated samples decreases from ~1700 to ~1200 J kg^{-1} K^{-1} with increasing density or, equivalently, as water-to-cement mass ratio is lowered from 0.5 to 0.3. Note that this increasing trend in c_p with increasing mixing w:c-ratio is the most pronounced under water saturated conditions but does occur in the (partially) dried samples as well.

4.2.3. Effects of cement type and additives

Figure 4 shows data for various types of neat cement, including ASTM CEM I cement at 22°C (diamonds – Kim and Oh, 2019; Kim et al., 2017), NIST CCRL Cement Proficiency Sample 152 at 23°C (squares and circles – Bentz, 2007) and ASTM CEM III/C 32.5 cement at 20°C (triangles – De Schutter and Taerwe, 1995). CEM I and CEM III cement can be considered comparable to API Class A and C cement, respectively (Table 1). Based on the limited experimental data available, the c_p of API Class C cement might be slightly higher than that of API Class A cement. Note these cements have different w:c-ratios, which could also explain the observed variation. More data would be needed before firm conclusions can be drawn with respect to the impact of cement type, but a preliminary analysis using thermodynamic models suggest the effect will be fairly minor (see Section 4.3.1 below). Note the foregoing concerns neat cements only, as c_p could possibly be augmented using additive materials with suitable volumetric heat capacity properties.

4.3. Estimation of specific heat capacity using thermodynamic models

When the mineralogical composition and porosity of fully set cement are known, its isobaric specific heat capacity, c_p [J kg^{-1} K^{-1}], can be estimated using a rule of mixtures and specific heat capacity data available for its constituent phases (Choktaweekarn et al., 2009; Qomi et al., 2015; Wadsö et al., 2012):

$$c_p = \sum_{i=1}^{n} m_i c_{p,i} \tag{8}$$

Here, $c_{p,i}$ [J kg^{-1} K^{-1}] and m_i [-] are specific heat capacities and mass fractions, respectively, of n different components that comprise the solid cement and pore fluid phase. Matschei et al. (2007) and Lothenbach

et al. (2008) provide standard molar thermodynamic properties for a wide range of Portland cement phases ($P = 0.1$ MPa, $T = 298.15$ K). These reference data can also be used to calculate specific heat capacities at higher temperatures (Anderson and Crerar, 1993; Lothenbach et al., 2008):

$$c_{p,i}(T) = \frac{1}{u_i}\left(\beta_{0,i} + \beta_{1,i}T + \beta_{2,i}T^{-2} + \beta_{3,i}T^{-0.5}\right) \quad (9)$$

Here, T [K] is temperature in Kelvin, u_i [kg mol^{-1}] is the molar mass of component i, and $\beta_{j,i}$ ($j = 0, 1, 2, 3$) are empirical coefficients that have been tabulated for various cement compounds (Cemdata07; Lothenbach et al., 2008; Matschei et al., 2007). A recent version of this thermodynamic database, covering temperatures of 0 to 99°C and pressures of 0.1 to 10 MPa, has been made available via a web application called CemGEMS (Cemdata18; Kulik et al., 2021).

4.3.1. Example calculations for neat API Classification cements

Given the scarcity of experimental data on the heat capacity of set cements of API classified compositions, we have estimated their c_p using the CemGEMS application (Kulik et al., 2021). To this end, we performed a number of simulations using typical clinker compositions and nominal mixing water-to-cement mass (w:c) ratios for the different API classes (Table 1) as listed by Nelson and Michaux (2006). CemGEMS was run in Minimal mode, assuming complete hydration, while varying temperature and pressure. In a second set of simulation runs, the temperature and pressure were fixed at 25°C and 10 MPa, while varying the slurry mixing w:c-ratio for each class. Figure 5a shows CemGEMS results for the specific heat capacity of API Class A, C, E and G cement, mixed to their nominal w:c-ratios, as a function of temperature at 10 MPa. The effect of pressure was investigated and found insignificant in the CemGEMS simulations (not shown). All API cements display a modest increase in specific heat capacity with increasing temperature. At their nominal mixing w:c-ratios, the c_p of API Class A and G cement are comparable (~1500 J kg^{-1} K^{-1}), whereas those of Class C and E cement appear higher and lower, respectively. When a wider range of w:c-ratios is considered, however, this variation is clearly attributable to differences in the nominal w:c-ratio of the different API classes (Table 1, Figure 5b), rather than differences in their clinker composition. Note the CemGEMS simulations yield c_p-values ranging 1200–1800 J kg^{-1} K^{-1} for w:c-ratios ranging from 0.3 to 0.6, which is in good agreement with lab data for saturated CEM I cement (blue diamonds – Figure 5b).

5. Thermal expansion behaviour

5.1. Basic definitions

Most materials tend to change their dimensions (shape, volume or density) when subjected to a change in temperature. Excluding changes resulting from phase transitions, this tendency is referred to as thermal expansion. Raising the temperature of a substance increases the average kinetic energy of its constituent atoms, causing them to move and vibrate more vigorously. Usually, this leads to an increase in the average interatomic distance, such that most materials expand when heated and contract when cooled. Dimensional change with temperature is often described in terms of a relative volume change:

$$\alpha_V = \left(\frac{\partial e_V}{\partial T}\right)_\sigma = \frac{1}{V}\left(\frac{\partial V}{\partial T}\right)_\sigma \quad (10)$$

Here, α_V [K^{-1}] is the volumetric coefficient of thermal expansion, e_V [-] is the volumetric strain, V [m^3] is the volume of material, and T [K] is temperature, while the subscript σ indicates thermal expansion is assumed to occur at constant stress (e.g., confining pressure). Similarly, a linear coefficient of thermal expansion, α_L [K^{-1}], can be defined:

$$\alpha_L = \left(\frac{\partial e_L}{\partial T}\right)_\sigma = \frac{1}{L}\left(\frac{\partial L}{\partial T}\right)_\sigma \quad (11)$$

Here, e_L [-] denotes linear strain and L [m] represents some length dimension of the material. For isotropic materials undergoing small strains and temperature changes, $\alpha_V \approx 3\alpha_L$. In anisotropic materials, α_L will have tensor properties, e.g., differ with crystallographic direction. Note α may vary with temperature and stress state. When the thermal expansion properties of adjacent materials are dissimilar, change in temperature can induce thermal stresses. This is particularly relevant for wells, where mismatches between the thermal strain responses of the steel casings, cement sheaths, and surrounding rock could lead to the generation of microannuli and other defects.

5.2. Thermal expansion and contraction in cementitious materials

The thermal expansion behaviour of low permeability, porous

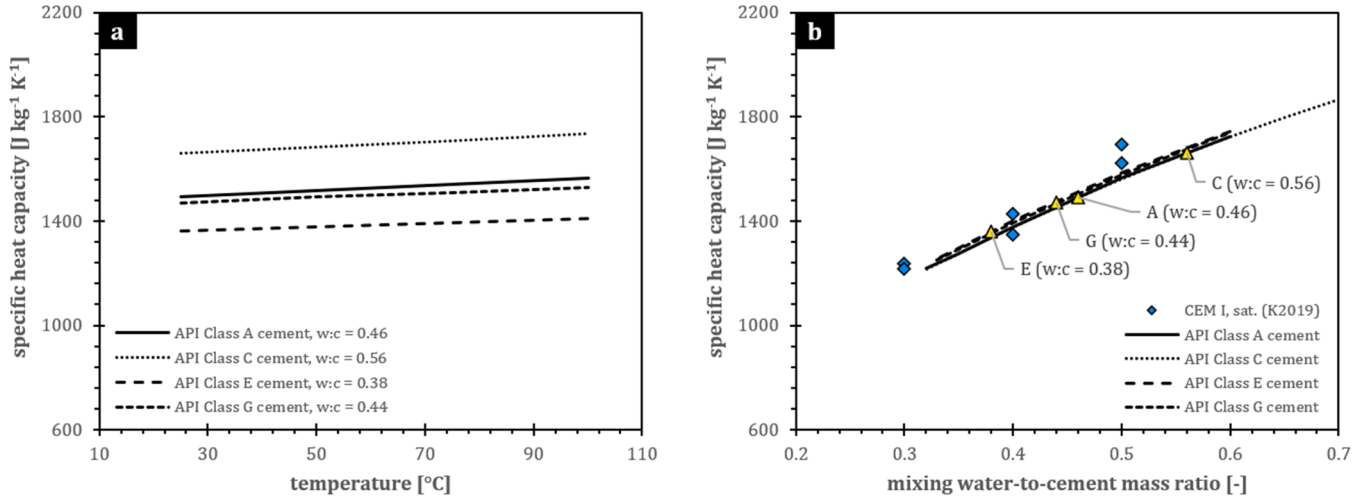

Figure 5. Specific heat capacity of water-saturated API classified neat cement compositions as a function of a) temperature and b) mixing water-to-cement mass ratio. Data were obtained from simulations run at 10 MPa pressure using the CemGEMS application (Kulik et al., 2021). Figure 5a shows c_p with temperature for API Class A, C, E and G cements, mixed at their nominal neat w:c-ratios (Table 1). Figure 5b shows c_p at 25°C as a function of w:c-ratio for API Class A, C, E, and G cement. Note the simulation results for different classes largely collapse into a single curve, demonstrating that the pattern in Figure 5a is caused by different nominal mixing w:c-ratios (indicated using yellow triangles) rather than by differences in clinker composition (Table 1). For comparison, lab measurements on water-saturated CEM I cement are plotted in blue (Kim and Oh, 2019; Kim et al., 2017).

materials such as cement is more complex than can be readily captured using the basic definitions above. Cement also exhibits a delayed response to changes in temperature, caused by mass transfer of water inside the cement (Bažant, 1970; Helmuth, 1961; Powers, 1958; Sellevold and Bjøntegaard, 2006). Among others, the thermal response of cement depends on i) the initial degree of pore fluid saturation, ii) pore fluid drainage conditions, and iii) the rate of heating or cooling (Bažant, 1970; Grasley and Lange, 2007; Helmuth, 1961; Meyers, 1951). Bažant (1970) provides a thermodynamic analysis of cement thermal expansion behaviour, considering various aspects related to redistribution of internal moisture. These effects include i) true thermal expansion of the solid skeleton of the cement matrix, ii) strains induced by chemical potential differences in the gel- and capillary-porewater and associated fluid transport, and iii) changes in relative humidity in any unsaturated capillary pore space (cf. Sellevold and Bjøntegaard, 2006). Since the coefficient of thermal expansion of aqueous fluids is much larger than that of the solid skeleton of the cement matrix, the effective volumetric response to heating will typically be a combination of true thermal expansion of the porous structure, and additional strain due to thermal pressurization of the pore fluid (Valenza II and Scherer, 2005). The latter effect dissipates over time, as flow redistributes the fluid and relieves the excess pore pressure (Bažant, 1970; Helmuth, 1961). Conversely, sudden cooling can lead to rapid contraction of the set cement, followed by a more gradual expansion as internal water gets redistributed or porewater is drawn in from the surroundings. For both cases, the rate of time-dependent deformation will depend on the cement matrix permeability and the proximity of a pore fluid sink or supply, i.e., the length scales over which pressure diffusion can take place (Ai et al., 2001; Bažant, 1970; Sellevold and Bjøntegaard, 2006).

Given the significant role of the pore fluid phase in the thermal behaviour of porous media, it is important to define the degree of pore fluid saturation and drainage conditions under which the coefficient of thermal expansion is evaluated in experiments. With respect to the latter, usually two endmember cases are identified, namely fully drained and fully undrained conditions. Under fully drained conditions, the pore fluid pressure is constant throughout heating-cooling. This corresponds to scenarios where the rate of temperature change is slow enough for pore fluid pressure changes to be effectively dissipated through in- or outflow of pore fluid. The coefficient of drained thermal expansion, α_d [K^{-1}], is defined as (Ghabezloo, 2010):

$$\alpha_d = \frac{1}{V}\left(\frac{\partial V}{\partial T}\right)_{\sigma,p_f} \tag{12}$$

Conversely, under fully undrained conditions, the heating-cooling process occurs at constant pore fluid mass (i.e., zero in- or outflow of pore fluid). In such scenarios, differences in thermal expansion of the pore fluid and solid skeleton can generate changes in pore fluid pressure plus associated deformation. The coefficient of undrained thermal expansion, α_u [K^{-1}], is defined as (Ghabezloo, 2010):

$$\alpha_u = \frac{1}{V}\left(\frac{\partial V}{\partial T}\right)_{\sigma,m_f} \tag{13}$$

where m_f [kg] denotes the mass of pore fluid in the cement. Undrained conditions occur when the thermal diffusivity exceeds pressure diffusivity, e.g., upon the relatively fast heating-cooling of low permeability materials, such that pore fluid pressure differences cannot be dissipated via flow.

The volumetric coefficients of thermal expansion under drained and undrained conditions can be related using thermo-poroelastic properties of the cement (Ghabezloo, 2010):

$$\alpha_u = \alpha_d + \varphi_0 B\left(\alpha_f - \alpha_\varphi\right) \tag{14}$$

Here, φ_0 [-] is the reference porosity, B [-] is Skempton's coefficient B, defined as the ratio of pore fluid pressure change over confining pressure change under undrained conditions (Skempton, 1954), and α_f and α_φ [K^{-1}] are the volumetric coefficients of drained thermal expansion of the pore fluid phase and the pore void volume, respectively (Ghabezloo, 2010; Ghabezloo et al., 2009).

5.3. Experimental thermal expansion data available in the literature

The amount of data available on thermal expansion of wellbore cements is relatively limited. Experiments to determine the coefficient of thermal expansion typically involve physical measurement of dimensional change (i.e., length or volume of a sample) in response to an imposed temperature change (Ghabezloo et al., 2009; Helmuth, 1961). In the following, we first discuss results from tests conducted under atmospheric pressure, considering trends with degree of pore fluid saturation, porosity, mixing water-to-cement mass ratio, slurry density, and temperature. Subsequently, we will discuss sparse measurement data on cement thermal expansion under elevated pressures. In the following, all thermal expansion data will be presented in terms of volumetric coefficients, assuming $\alpha_V \approx 3\alpha_L$ for the conversion of any results originally reported as linear coefficients. For strains, expansions and elongations are denoted positive.

5.3.1. Thermal response of submerged, water-saturated cement at ambient pressure

Among experiments conducted at atmospheric pressure, those on water-saturated, submerged cement samples are probably the most representative for wellbore conditions. Helmuth (1961) extensively studied the thermal expansion behaviour of neat ASTM CEM I cement 15754 (comparable to API Class A), prepared using mixing water-cement mass ratios of 0.43 to 0.61, and cured at 23°C. The measurements were performed on initially water-saturated samples submerged in kerosine, by varying the temperature between 0-25°C, using ramps of 15-30°C h^{-1}, while monitoring sample length. Selected data of Helmuth (1961) have been reproduced in Figure 6. Under cooling and heating at 15°C h^{-1} without interruption (i.e., temperature versus time plots as a triangular wave), the specimens' strain response shows hysteresis loops. The hysteresis is more pronounced at lower water-to-cement mass ratios (Figure 6a-b) but does not vary much with pre-equilibration temperature (compare light and dark grey curves in Figure 6a). Calculating the local slope of the strain-temperature curves yields apparent coefficients of thermal expansion that show markedly higher dynamic values (due to lag between the imposed temperature change and volumetric response) but bottom out around ~3 × 10^{-5} K^{-1} (Figure 6c). In another experiment, Helmuth (1961) subjected cement (w:c ratio = 0.55) to thermal cycles incorporating hold periods, during which the sample was maintained under isothermal conditions (Figure 6d). Note that the thermal response includes recovery during subsequent holds, while the strain "overshoot" at the end of an imposed ramp increases with faster temperature change rate (compare first and second cycle in Figure 6e). The dashed blue curve in Figure 6d connects the initial and thermally equilibrated strain states, yielding an apparent volumetric coefficient of 3.84 × 10^{-5} K^{-1}, which has been used to construct the corresponding blue curves in Figure 6e-f. Overall, the data show that thermal pressurization and the delayed response due to mass transfer of cement porewater tend to increase instantaneous strains and the local slope of strain-temperature data (Figure 6f).

5.3.2. Thermal response of cement under relative humidity at ambient pressure

The majority of experimental results obtained at atmospheric pressure involve samples equilibrated with air of a specific relative humidity (RH) (Meyers, 1951; Powers, 1958; Sabri and Illston, 1982; Wittmann and Lukas, 1974). While slight deviations from saturation may arise from changes in dissolved salt content of the pore fluid (e.g., Raoult's law), or from surface tension and capillary effects (e.g., Kelvin equation), significantly lowered RH conditions are unlikely to occur in wellbore cement, given the usual availability of water and quasi-closed

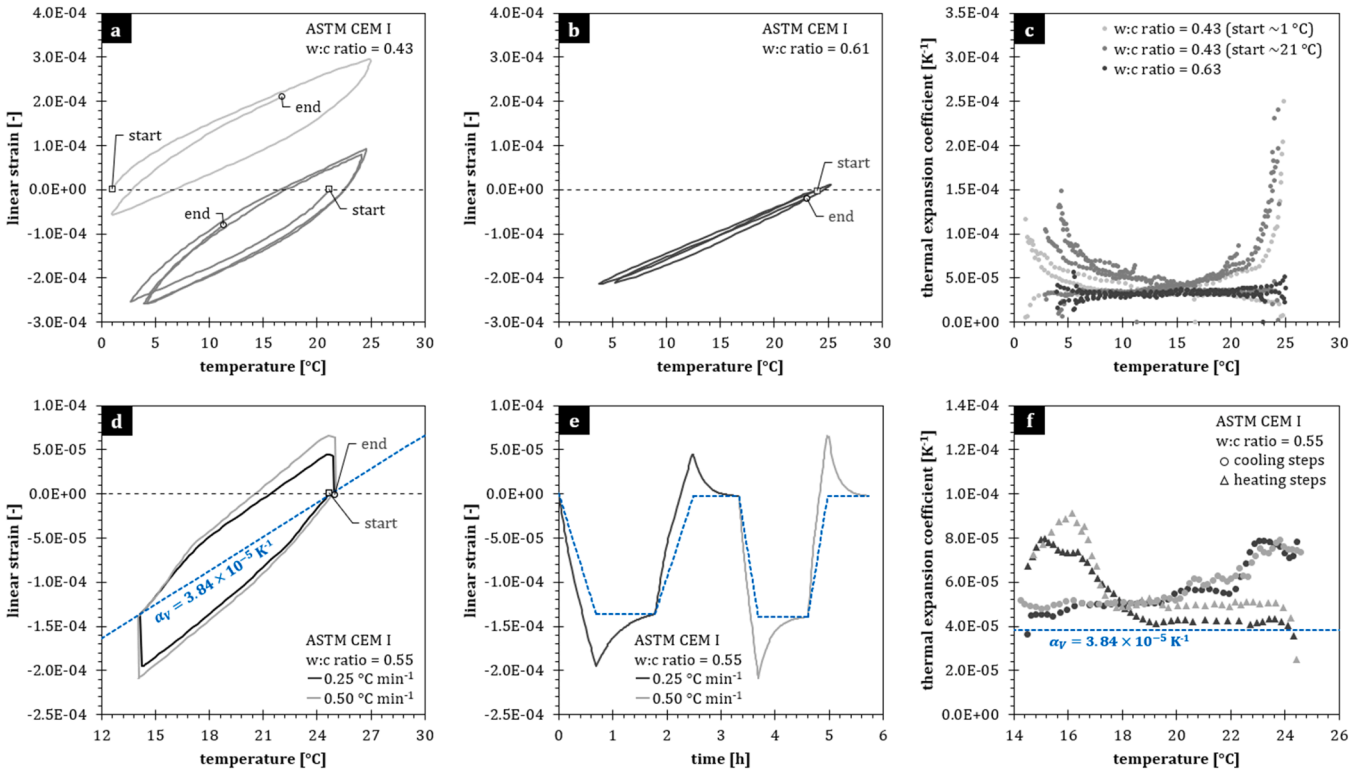

Figure 6. Thermal response of water-saturated ASTM CEM I cement cured at 23°C (Helmuth, 1961), with a-b) linear strain versus temperature during cycles of cooling and heating at 15°C h^{-1} for samples with water-to-cement mass ratios of a) 0.43 and b) 0.61, with c) corresponding apparent volumetric coefficients of thermal expansion; d-e) strain-temperature and strain-time data for cement (w:c ratio of 0.55) subjected to two thermal cycles that incorporate isothermal periods, showing the delayed response and transient behaviour during the isothermal periods. Blue dashed curves in d-e) connect equilibrated strains at the ends of isothermal periods, yielding an apparent volumetric coefficient of thermal expansion of 3.84 × 10^{-5} K^{-1}; f) corresponding volumetric coefficients based on local slope of the measured strain-temperature data. Note plot e) was reconstructed using data from Figure 7 and Table 2 of Helmuth (1961).

system conditions at depth (Badino, 2010). Nevertheless, results obtained at relatively high RH (say >85%) can show relevant trends, while those obtained at lower RH, though not directly applicable to downhole situations, may still be useful for comparative purposes.

5.3.2.1. Effects of relative humidity. Meyers (1951) studied the thermal expansion behaviour of neat ASTM CEM I cement as a function of RH and internal state of moisture. Theye found that α is low at low RH, increases with intermediate RH, and then decreases again, reaching a minimum at 100% RH or water-saturated conditions (Figure 7a). This effect at intermediate saturations is observed in a wide range of cementitious compounds (Mitchell, 1953; Powers, 1958; Sabri and Illston, 1982) and has been attributed to hygrothermal strain and internal RH change (Bažant, 1970; Sellevold and Bjøntegaard, 2006). Meyers (1951) noted variation in α with RH diminishes with increasing age of the cement. They further found variation with RH decreased with lower C-S-H phase content, suggesting factors such as gel nanostructure or pore size are important. It should be noted here that changes in RH at constant temperature also produce considerable volume changes in cement due to surface stress effects (Hansen, 1987). According to an analysis by Sellevold and Bjøntegaard (2006), strains associated with temperature change-induced variations in RH could largely explain the increased α observed at intermediate saturations.

5.3.2.2. Effects of cement composition. Mitchell (1953) determined coefficients of thermal expansion for a wide range of cement compositions in terms of C3S, C2S, C3A, and C4AF content [wt.%]. The RH-effect is qualitatively similar to that found by Meyers (1951) for ASTM CEM I cement (Figure 7a). Plotting α_V as function of cement clinker composition reveals a weak trend with C3A content (Figure 7e), but the variations remain small compared to other factors such as transient effects (compare Figure 6f). It should be noted, however, that Mitchell (1953) prepared his samples at water-to-cement mass ratios of 0.25-0.35, i.e., values lower than typical for wellbore cement (Table 1). Shui et al. (2010) report thermal expansion data for P.O. 42.5 Portland cement with various mineral additives. Their cement was cured under RH >95% and 20°C for 28 days. Their tests were performed in air with controlled RH of >85%, heating specimens to 85°C while monitoring length change. They found the maximum recorded coefficient of thermal expansion increased with increasing portlandite content of the hydrated cement (see Table 4 of Shui et al., 2010). These results are shown in Figure 7f, together with the volumetric coefficient of thermal expansion of pure portlandite as calculated from thermodynamic data (Qomi et al., 2015).

5.3.3. Effects of slurry density, porosity, and mixing water-to-cement mass ratio

Cuello Jimenez et al. (2017) performed measurements on API Class H cements prepared using water-to-cement mass ratios ranging 0.26-0.69, corresponding to slurry densities between 2190 and 1680 kg m^{-3}. They also preformed tests on foamed cements, extending their investigated density range down to 1140 kg m^{-3}. The tests were performed using an Anter Unitherm Model 1101 dilatometer, increasing the temperature from 25°C to 100°C at 12°C h^{-1}, while measuring change in sample length, subsequently calculating averaged α_L for the explored range from the slope of thermal strain versus temperature. Cuello Jimenez et al. (2017) do not specify the degree of pore fluid saturation during the thermal expansion measurements in their paper, and therefore the data are plotted in white (Figure 8). The linear coefficients reported by Cuello Jimenez et al. (2017) fall in the range of 4.3 × 10^{-6} to 1.1 × 10^{-5} K^{-1}, corresponding to volumetric coefficients of 2.3-5.6 × 10^{-5}

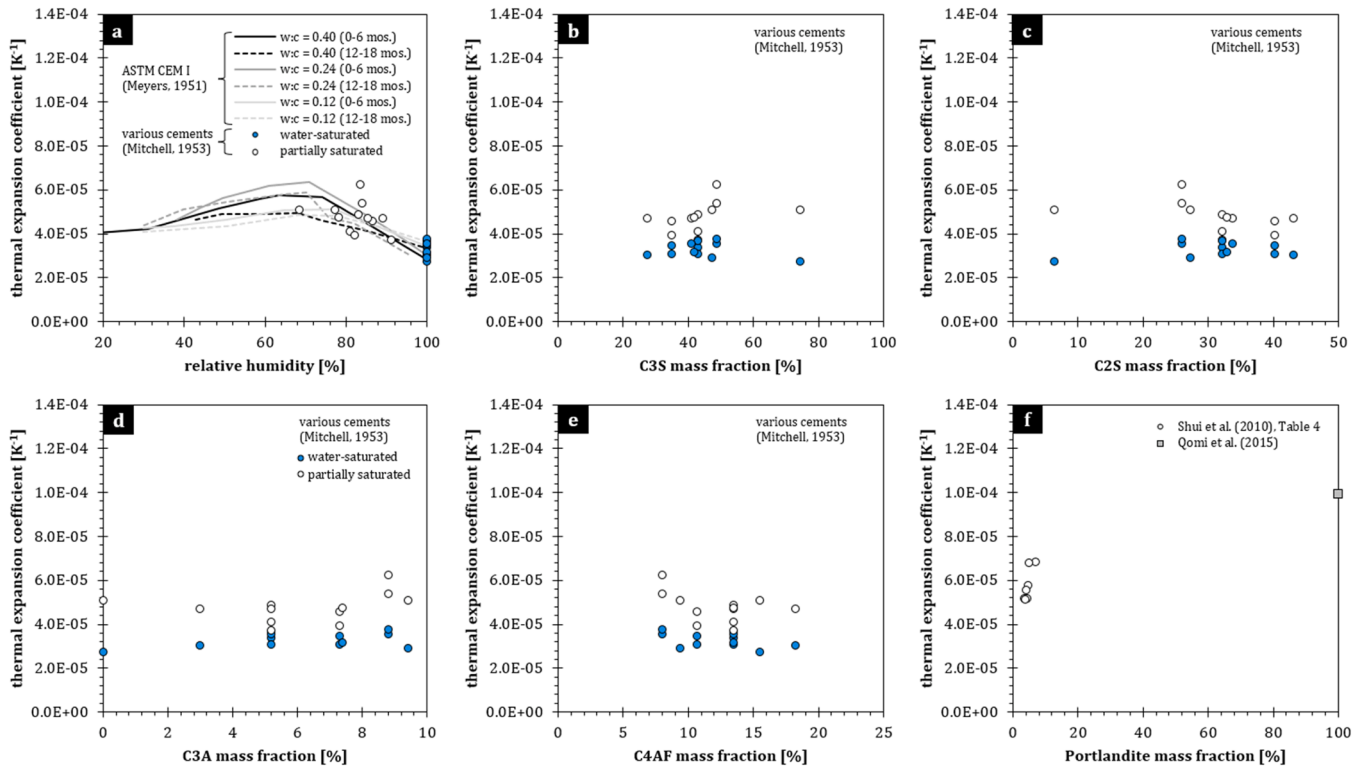

Figure 7. Volumetric coefficients of thermal expansion of Portland-based cement as function of a) relative humidity, b) C3S mass fraction in the clinker, c) C2S mass fraction in the clinker, d) C3A mass fraction in the clinker, e) C4AF mass fraction in the clinker, and f) Portlandite mass fraction in the hydrated cement. Data plotted in blue represent water-saturated conditions, those plotted in white intermediate saturations. Plots include experimental data from Meyers (1951), Mitchell (1953) and Shui et al. (2010), and model simulation results from Qomi et al. (2015).

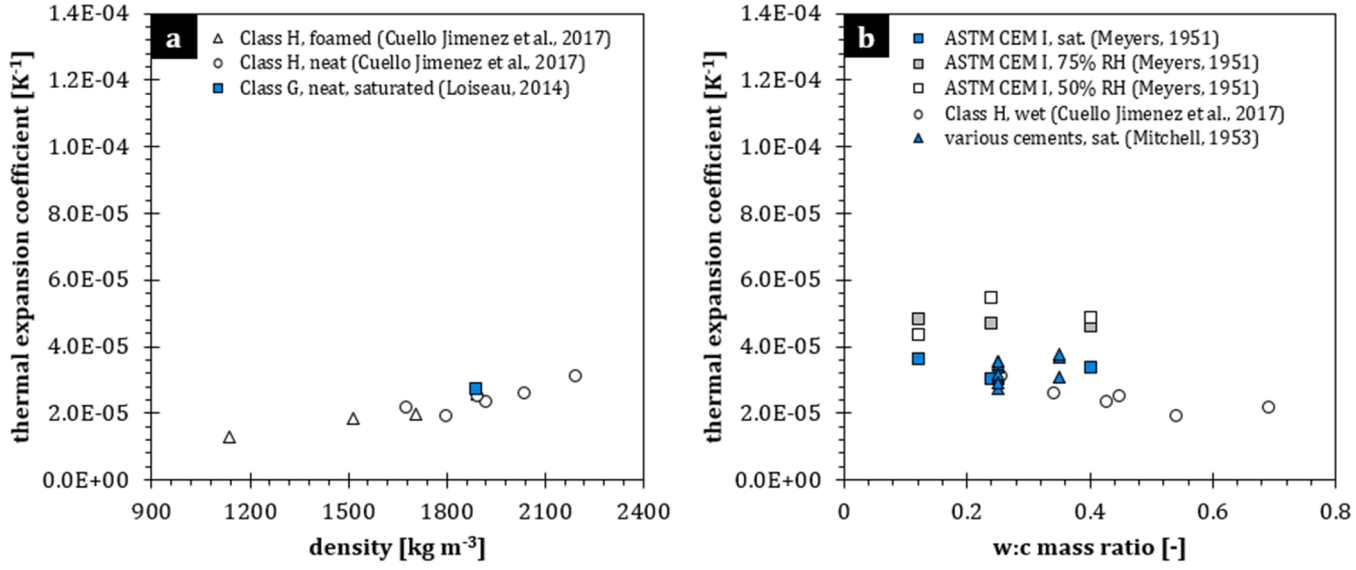

Figure 8. Volumetric coefficients of thermal expansion for ASTM CEM I cement (squares) and API Class H cement (neat as circles, foamed as triangles), as functions of a) slurry density and b) water-to-cement mass ratio. Plot includes data from Meyers (1951), Mitchell (1953), Loiseau (2014) and Cuello Jimenez et al. (2017). Data for water-saturated samples plotted in blue, partially saturated cement shown in white and grey. Note that, although the data of Cuello Jimenez et al. (2017) are plotted in white on basis of the information available in the publication (degree of saturation unknown), their samples were likely close to fully saturated (W. Cuello Jimenez, pers. comm., April 2023), i.e., conditions similar to data plotted In blue.

K^{-1} (assuming $\alpha_V \approx 3\alpha_L$). These values are similar to those reported my Meyers (1951) and Mitchell (1953) for water-saturated cement. Interestingly, this contrasts with the λ data of Cuello Jimenez et al. (2017), which showed indications of drying during measurement (see Section 3.2.2). Enquiry about this confirmed that the samples used for thermal expansion testing were near-saturated at the start and enclosed in glass cells during measurement, making drying-effects less likely here than in the λ measurements (W. Cuello Jimenez, pers. comm., April 2023). In any case, the data of Cuello Jimenez et al. (2017) demonstrate decreasing trends in α with decreasing density (Figure 8a) and

increasing w:c ratio (Figure 8b). Shui et al. (2010) report trends with porosity, where the differences between samples are related to mineral admixtures. They observed decreasing α with increasing porosity due to addition of fly ash and ground blast furnace slag, while porosity increase associated with addition of silica flour resulted in increased thermal expansion (see Figure 4 of Shui et al., 2010).

It should be noted that these decreasing trends with increasing porosity and water-to-cement mass mixing ratio are quite curious. Based on thermo-poroelastic theory, both the drained and undrained coefficients of thermal expansion of porous media normally increase with increasing porosity (Ghabezloo, 2010). The observed trends may represent artefacts related to drainage, e.g., possibly the more porous samples are easier to drain, or could reflect some microstructural or chemical changes particular to Portland cement, e.g., changes in the C-S-H gel pore size distribution. In any case, this atypical behaviour is generally not seen in porous media (Ghabezloo, 2010).

5.3.4. Thermal response in measurements performed at elevated pressure

Thus far we considered data obtained at ambient pressure. Meanwhile, wellbore cements will generally be subjected to elevated pressure conditions downhole. Ghabezloo et al. (2009) studied the thermal expansion behaviour of API Class G cement, prepared using a water-to-cement mass ratio of 0.44, at elevated pressure under both drained and undrained conditions. The drained experiment was performed under a confining pressure of 1.5 MPa and a constant pore fluid pressure of 1.0 MPa, heating the cement sample from 18°C to 87°C at a rate of 4.8°C h^{-1}, evaluating the drained coefficient of thermal expansion as the slope of volumetric strain with temperature, yielding a α_d of 6×10^{-5} K^{-1} (Figure 9). Note this value is significantly higher than typical experimental results obtained at ambient pressure (compare Figure 6-8).

The undrained experiment was performed under 19 MPa confining pressure, allowing the cement sample to equilibrate at confinement for two days before initiating thermal testing in order to minimize the impact of compaction creep processes. After stabilization, temperature was increased at 6°C h^{-1} while monitoring pore fluid pressure and bulk volumetric strain. During the heating stage, the thermal response of the cement sample was characterized by a α_u of 9.6×10^{-5} K^{-1} and a thermal pressurization coefficient of 0.62 MPa K^{-1} (Ghabezloo et al., 2009). Note these values are valid only up to 54°C, at which point the pore fluid pressure started to approach the confining pressure, causing deviating behaviour. During the cooling stage, the volume-temperature curve gradually steepened until a slope of $\alpha_u = 1.2 \times 10^{-4}$ K^{-1} was attained (Figure 9a). Final volumetric strain showed ~5×10^{-4} net compaction and a 1.7 MPa increase in pore fluid pressure. Similar to the hysteresis effects observed at ambient pressure, thermal cycling under elevated pressures leads to pore fluid pressure gradients, which increase the apparent thermal response. Note, however, that the background coefficient values increase with pressure (compare Figure 6f with 9b).

5.3.5. Effects of elevated and low temperatures

The coefficient of thermal expansion of most materials varies with temperature. For Portland cement this temperature dependence must be evaluated with the utmost care. Measurement artefacts may arise from many factors, e.g., due to changes in relative humidity during testing at ambient pressure, or from thermal pressurization of the pore fluid phase during testing at elevated pressure. More importantly, however, profound changes in Portland cement chemistry occur with temperature, such that exposure of set cement to large temperature sweeps or changes can result in phase instabilities. A well-known example is so-called "strength retrogression" at temperatures above about 110°C, which is believed to be caused by recrystallization of the C-S-H gel phase (Reddy et al., 2016; Zhu, 2019). While cement systems can be designed for application at elevated temperatures (e.g., ground quartz silica is usually added to formulations deployed above 100°C to help prevent strength retrogression), such systems may nevertheless undergo changes in their hydrated phase composition when temperature is varied. If the experimentally investigated temperature range contains significant phase boundaries, then this could potentially induce undetermined discontinuities in the cement thermal properties.

Bu et al. (2017) report thermal expansion coefficients for cement as a function of temperature up to 300°C, for what they refer to as "dry conditions". They state the coefficient of thermal expansion decreases above 45°C and even attains negative values at temperatures around 120°C. However, it should be noted that Bu et al. (2017) performed their tests at ambient pressure without controlling RH, thus allowing severe drying-effects and possibly even recrystallization or thermal decomposition of cement phases to occur. Whether such effects and the associated negative coefficients of thermal expansion are representative for downhole behaviour is highly questionable. Shui et al. (2010) report length change versus temperature for P.O. 42.5 cement samples up to 85°C (see Figure 1 of Shui et al., 2010). While these authors report only temperature-averaged coefficients (see Figure 2 of Shui et al., 2010),

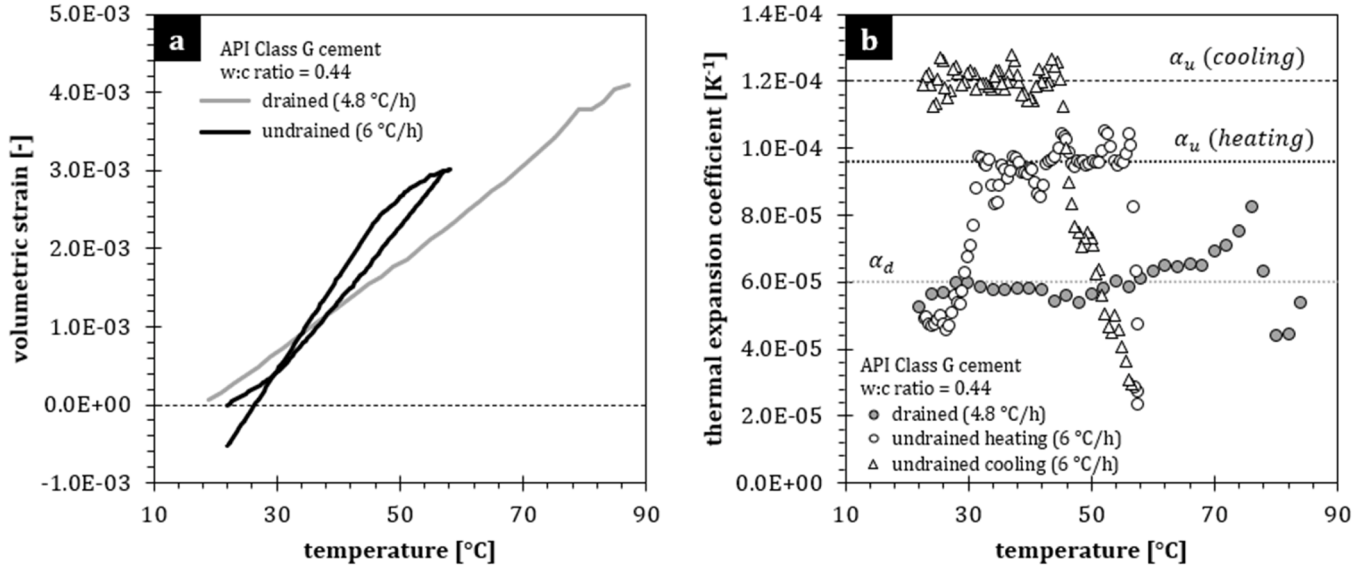

Figure 9. Thermal response of API Class G cement to heating under elevated confining and pore fluid pressure (Ghabezloo et al., 2009), with a) volumetric strain-temperature curves for drained and undrained conditions, and b) corresponding estimated for α_d and α_u, calculated as the local slope of the data in Figure 9a.

plotting the slope of their linear strain versus temperature data yields α that diminish rapidly above 60°C (Figure 10). Shui et al. (2010) performed their measurements in air of >85% RH. It is unclear whether RH was controlled at the actual test temperature or not. It should be noted that controlling RH using a salt-brine equilibrium at some reference temperature could have yielded lower RH at the higher test temperature. By contrast, loss of moisture is much less likely to occur under the elevated pressures encountered downhole. For example, Ghabezloo et al. (2009) recorded positive coefficients of thermal expansion over temperatures up to 86°C in their drained test under 1.5 MPa confining pressure. While recrystallization and other phase changes may still occur upon downhole exposure to increased temperatures, note that elevated pressures generally tend to suppress thermal decomposition reactions and extend the stable temperature range of hydrated phases.

A limited number of experimental studies has considered thermal expansion at low temperature. Helmuth (1961) studied ASTM CEM I cement volume change down to –25°C, noting that capillary porosity "emptied" by thermal contraction of the fluid during cooling towards freezing temperatures tended to liberate space to accommodate subsequent volumetric expansion upon pore fluid freezing, thus providing some protection against damage from frost heave. Similarly, Wittmann and Lukas (1974) studied a Portland cement known as "PZ 350 F (DIN 1164)", exploring thermal expansion behaviour as a function of degree of pore fluid saturation and temperature. They found that the thermal expansion coefficient of water-saturated cement decreases between 10°C and 0°C and increases again at subzero temperatures. For partially saturated cement, Wittmann and Lukas (1974) reported α decreases with lower temperatures (Figure 10). We were unable to find any cooling experiments or low-temperature data obtained under elevated pressure conditions.

6. Recommendations for numerical simulation of thermal effects in CCS wells

This literature review provides an overview of available experimental data and theoretical values for the thermal properties of Portland-based wellbore cements. The aim was to provide constraints on the ranges of these parameters for numerical model analyses of wellbore thermal behaviour under specific injection scenarios. The considered cement properties include its i) thermal conductivity and diffusivity, ii) specific heat capacity, and iii) coefficient of thermal expansion. Our literature survey revealed that the values obtained for these parameters in lab experiments depend strongly on test conditions and show significant ranges, e.g., differ by over half an order of magnitude in the case of thermal conductivity and thermal expansion coefficients. In particular, the degree of pore fluid saturation (internal moisture content) has a significant impact on all three properties studied. Confident use of lab values in numerical modelling analyses of wellbore integrity therefore requires careful consideration of the methods employed in the lab experiments (e.g., if samples can dry out during testing, then the values obtained may not be suitable for simulation of downhole conditions). Based on our review, we can conclude the following:

The **thermal conductivity** (λ) of Portland cements varies between 0.3 and 1.3 W m^{-1} K^{-1}. The degree of pore fluid saturation is one of the key controlling parameters, with higher saturations yielding larger λ. Water-saturated cement has λ of 0.9-1.3 W m^{-1} K^{-1}. Thermal conductivity increases with increasing cement density and decreases with increasing porosity and mixing water-to-cement mass ratio (Figure 1). Some experimental studies report an apparent decrease with increasing temperature, but this is likely an artefact of samples drying out during testing. Molecular-dynamics modelling of C-S-H gel phases suggests λ will not vary strongly with temperature. Based on the limited available data, no significant variation in λ with Portland cement clinker composition is expected (Table 1).

The **specific heat capacity** (c_p) of Portland cements varies between 900 and 2100 J kg^{-1} K^{-1}. Specific heat capacity increases with increasing degree of pore fluid saturation and mixing water-to-cement mass ratio, while c_p tends to decrease with increasing density and extent of hydration (Figure 4). Thermodynamic modelling shows that the c_p of water-saturated cement ranges 1200-1800 J kg^{-1} K^{-1}, displaying a slight increase with increasing temperature, and variation among API classified cements. However, modelling further shows this variation is chiefly due to differences in the nominal mixing water-to-cement mass ratios of API Class A-H cements (Figure 5).

The volumetric **coefficient of thermal expansion** (α_V) is more difficult to constrain because the response of Portland cement to temperature changes includes delayed effects associated with mass transfer of internal water, e.g., from the capillary porosity to the gel porosity or vice versa (Figure 6). Due to these processes, the degree of pore fluid saturation is a key controlling parameter (Figure 7). Estimates for α_V

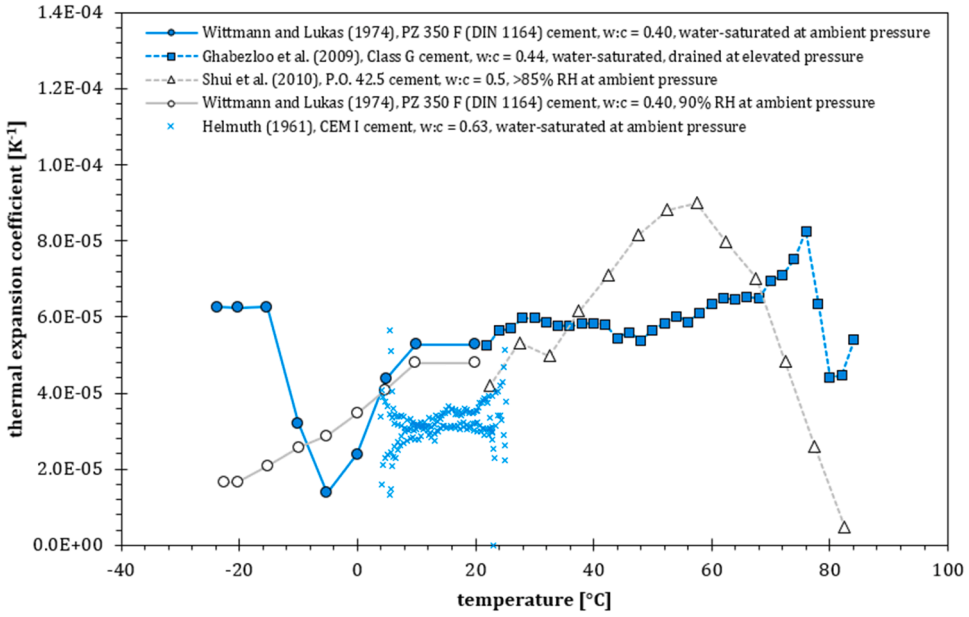

Figure 10. Coefficient of thermal expansion of Portland cement as a function of temperature. Data plotted in blue represents measurements performed under initially water-saturated conditions. Plot includes data from Helmuth (1961), Wittmann and Lukas (1974), Ghabezloo et al. (2009) and Shui et al. (2010).

under slow temperature change rates (i.e., assuming mass transfer of water can keep up: drained conditions) vary between 2×10^{-5} and 8×10^{-5} K^{-1}. The apparent thermal expansion coefficient tends to increase with increasing temperature change rate. Values for α_V obtained are minimal under water-saturated conditions. Variations in α_V with composition seem to be small compared to other factors (Figure 7). Some experimental studies report an apparent decrease in α_V with increasing temperature, but these observations are probably associated with samples drying out extensively during testing and are therefore considered unrepresentative for downhole behaviour. Based on very limited data obtained under elevated pressures, α_V remains nearly constant between 10°C and 90°C under drained conditions. Under undrained conditions, where no transfer of pore fluid is possible, measurement at elevated pressures yields considerably higher volumetric coefficients of thermal expansion, with steady values of up to 1.2×10^{-4} K^{-1} being registered (Figure 9). The intricate interplay between thermal (de)pressurization of the pore fluid phase and cement effective thermal expansion-contraction properties warrants further study.

CRediT authorship contribution statement

T.K.T. Wolterbeek: Conceptualization, Investigation, Visualization, Writing – original draft, Writing – review & editing. **S.J.T. Hangx:** Writing – review & editing.

Declaration of Competing Interest

The authors declare that they have no known competing financial interests or personal relationships that could have appeared to influence the work reported in this paper.

Data availability

Data used for the construction of figures in this review are available in the respective source documents cited.

Acknowledgements

We would like to thank two anonymous reviewers for their constructive and detailed feedback, which greatly helped us improve our manuscript. We also like to thank Walmy Cuello Jimenez for a pleasant discussion, which helped clarify some experimental specifics of their measurements. This study was funded by Shell Global Solutions International B.V. under Amended Contract PT63253-A2.

References

Acevedo, L., Chopra, A., 2017. Influence of Phase Behaviour in the Well Design of CO_2 Injectors. Energy Procedia 114, 5083–5099.
Ai, H., Young, J.F., Scherer, G.W., 2001. Thermal expansion kinetics: method to measure permeability of cementitious materials: II, application to hardened cement pastes. J. Am. Ceram. Soc. 84, 385–391.
Albawi, A., 2013. Influence of thermal cycling on cement sheath integrity. Institutt for petroleumsteknologi og anvendt geofysikk.
Anderson, G.M., Crerar, D.A., 1993. Thermodynamics in geochemistry: the equilibrium model. Oxford University Press on Demand.
Asadi, I., Shafigh, P., Hassan, Z.F.B.A., Mahyuddin, N.B., 2018. Thermal conductivity of concrete–A review. J. Build. Eng. 20, 81–93.
Asamoto, S., Le Guen, Y., Poupard, O., Capra, B., 2013. Well integrity assessment for CO_2 injection: A numerical case study on thermo-mechanical behavior in downhole CO_2 environments. Eng. Comput. 30 (6), 842–853.
Bachu, S., 2008. CO_2 storage in geological media: Role, means, status and barriers to deployment. Prog. Energy Combust. Sci. https://doi.org/10.1016/j.pecs.2007.10.001.
Badino, G., 2010. Underground meteorology-"What's the weather underground? Acta carsologica 39 (3), doi.org/10.3986/ac.v39i3.74.
Baghban, M.H., Hovde, P.J., Jacobsen, S., 2013. Analytical and experimental study on thermal conductivity of hardened cement pastes. Mater. Struct. 46, 1537–1546.
Baghban, M.H., Kioumarsi, M., Grammatikos, S., 2018. Prediction Models for Thermal Conductivity of Cement Based Composites. Nord. Concr. Res. 58, 163–171.
Bažant, Z.P., 1970. Delayed thermal dilatations of cement paste and concrete due to mass transport. Nucl. Eng. Des. 14, 308–318.
Belfroid, S., Koenen, M., Kreft, E., Huijskes, T., Neele, F.. CCS at Depleted Gas Fields in North Sea: Network Analysis. https://dx.doi.org/10.2139/ssrn.3813026.
Bentz, D.P., 2007. Transient plane source measurements of the thermal properties of hydrating cement pastes. Mater. Struct. 40, 1073–1080.
Bois, A.-P., Vu, M.-H., Ghabezloo, S., Sulem, J., Garnier, A., Laudet, J.-B., 2013. Cement sheath integrity for CO_2 storage–An integrated perspective. Energy Procedia 37, 5628–5641.
Bois, A.-P., Vu, M.-H., Noël, K., Badalamenti, A., Delabroy, L., Thérond, E., Hansen, K., 2018. Cement plug hydraulic integrity-the ultimate objective of cement plug integrity. SPE Norway One Day Seminar. Society of Petroleum Engineers. https://doi.org/10.2118/191335-MS.
Breuer, S., Schwotzer, M., Speziale, S., Schilling, F.R., 2020. Thermoelastic properties of synthetic single crystal portlandite $Ca(OH)_2$-Temperature-dependent thermal diffusivity with derived thermal conductivity and elastic constants at ambient conditions. Cem. Concr. Res. 137, 106199.
Bu, Y., Chang, Z., Du, J., Liu, D., 2017. Experimental study on the thermal expansion property and mechanical performance of oil well cement with carbonaceous admixtures. RSC Adv 7, 29240–29254.
Carey, J.W., 2013. Geochemistry of wellbore integrity in CO_2 sequestration: Portland cement-steel-brine-CO_2 interactions. Rev. Mineral. Geochemistry 77, 505–539.
Carslaw, H.S., Jaeger, J.C., 1947. Conduction of heat in solids. Oxford at the Clarendon Press.
Choi, Y.-S., Young, D., Nešić, S., Gray, L.G.S., 2013. Wellbore integrity and corrosion of carbon steel in CO_2 geologic storage environments: A literature review. Int. J. Greenh. Gas Control 16, S70–S77.
Choktaweekarn, P., Saengsoy, W., Tangtermsirikul, S., 2009. A model for predicting thermal conductivity of concrete. Mag. Concr. Res. 61, 271–280.
Cuello Jimenez, W., Pang, X., Urdaneta, J.A., Sørensen, E., Lende, G., Nimane, S., 2017. Thermo-mechanical properties of annular sealants—A path to optimized wellbore integrity and economics. In: SPE Kuwait Oil & Gas Show and Conference. OnePetro.
De Andrade, J., Sangesland, S., Todorovic, J., Vrålstad, T., 2015. Cement sheath integrity during thermal cycling: a novel approach for experimental tests of cement systems. SPE Bergen One Day Seminar. Society of Petroleum Engineers.
De Schutter, G., Taerwe, L., 1995. Specific heat and thermal diffusivity of hardening concrete. Mag. Concr. Res. 47, 203–208.
Dou, H., Dong, X., Duan, Z., Ma, Y., Gao, D., 2020. Cement Integrity Loss due to Interfacial Debonding and Radial Cracking during CO_2 Injection. Energies 13. https://doi.org/10.3390/en13174589.
Dusseault, M.B., Gray, M.N., Nawrocki, P.a, 2000. Why oilwells leak: Cement behavior and long-term consequences. In: SPE International Oil and Gas Conference and Exhibition, SPE 64733, p. 8. https://doi.org/10.2118/64733-MS.
Engineering Toolbox, 2004. Ice - Thermal properties [WWW Document]. URL https://www.engineeringtoolbox.com/ice-thermal-properties-d_576.html (accessed 9.8.21).
Fan, D., Yang, S., 2018. Mechanical properties of CSH globules and interfaces by molecular dynamics simulation. Constr. Build. Mater. 176, 573–582.
García, A., Contreras, E., Viggiano, J.C., 1989. Establishment of an empirical correlation for estimating the thermal conductivity of igneous rocks. Int. J. Thermophys. 10, 1063–1074.
Gasda, S.E., Bachu, S., Celia, M.A., 2004. Spatial characterization of the location of potentially leaky wells penetrating a deep saline aquifer in a mature sedimentary basin. Environ. Geol. 46, 707–720. https://doi.org/10.1007/s00254-004-1073-5.
Ghabezloo, S., Shui, ZH, Zhang, R., Chen, W., Xuan, D., 2010. Effect of porosity on the thermal expansion coefficient: A discussion of the paper 'Effects of mineral admixtures on the thermal expansion properties of hardened cement paste. Constr. Build. Mater. 24 (9), 1761, 1796–1798.
Ghabezloo, S., Sulem, J., Saint-Marc, J., 2009. The effect of undrained heating on a fluid-saturated hardened cement paste. Cem. Concr. Res. 39, 54–64.
Godec, M., Kuuskraa, V., Van Leeuwen, T., Melzer, L.S., Wildgust, N., 2011. CO_2 storage in depleted oil fields: The worldwide potential for carbon dioxide enhanced oil recovery. Energy Procedia 4, 2162–2169.
Grasley, Z.C., Lange, D.A., 2007. Thermal dilation and internal relative humidity of hardened cement paste. Mater. Struct. 40, 311–317.
Gu, T., Guo, X., Li, Z., Cheng, X., Fan, X., Korayem, A., Duan, W.H., 2017. Coupled effect of CO_2 attack and tensile stress on well cement under CO_2 storage conditions. Constr. Build. Mater. 130, 92–102. https://doi.org/10.1016/j.conbuildmat.2016.10.117.
Hamza, A., Hussein, I.A., Al-Marri, M.J., Mahmoud, M., Shawabkeh, R., Aparicio, S., 2021. CO_2 enhanced gas recovery and sequestration in depleted gas reservoirs: A review. J. Pet. Sci. Eng. 196, 107685.
Hangx, S.J.T., van der Linden, A., Marcelis, F., Liteanu, E., 2015. Defining the brittle failure envelopes of individual reaction zones observed in CO_2-exposed wellbore cement. Environ. Sci. Technol. 50, 1031–1038. https://doi.org/10.1021/acs.est.5b03097.
Hansen, O., Gilding, D., Nazarian, B., Osdal, B., Ringrose, P., Kristoffersen, J.-B., Eiken, O., Hansen, H., 2013. Snøhvit: The history of injecting and storing 1 Mt CO_2 in the fluvial Tubåen Fm. Energy Procedia 37, 3565–3573.
Hansen, W., 1987. Drying shrinkage mechanisms in portland cement paste. J. Am. Ceram. Soc. 70 (5), 323–328.
Hashin, Z., Shtrikman, S., 1962. A variational approach to the theory of the elastic behaviour of polycrystals. J. Mech. Phys. Solids 10, 343–352.
He, Y., 2005. Rapid thermal conductivity measurement with a hot disk sensor: Part 1. Theoretical considerations. Thermochim. Acta 436, 122–129.

Heathman, J.F., Beck, F.E., 2006. Finite Element Analysis Couples Casing and Cement Designs for HTHP Wells in East Texas. In: IADC/SPE Drilling Conference. Society of Petroleum Engineers.
Helmuth, R.A., 1961. Dimensional changes of hardened Portland cement pastes caused by temperature changes. Highw. Res. Board Proc. 40, 315–336.
Hepple, R.P., Benson, S.M., 2005. Geologic storage of carbon dioxide as a climate change mitigation strategy: performance requirements and the implications of surface seepage. Environ. Geol. 47, 576–585. https://doi.org/10.1007/s00254-004-1181-2.
Hong, S.-N., Yu, C.-J., Hwang, U.-S., Kim, C.-H., Ri, B.-H., 2020. Effect of porosity and temperature on thermal conductivity of jennite: A molecular dynamics study. Mater. Chem. Phys. 250, 123146.
Hoteit, H., Fahs, M., Soltanian, M.R., 2019. Assessment of CO_2 injectivity during sequestration in depleted gas reservoirs. Geosciences 9, 199.
Huan, X., Xu, G., Zhang, Y., Sun, F., Xue, S., 2021. Study on Thermo-Hydro-Mechanical Coupling and the Stability of a. Geothermal Wellbore Structure. Energies 14. https://doi.org/10.3390/en14030649.
Ichim, A., Teodoriu, H.C., 2017. Investigations on the surface well cement integrity induced by thermal cycles considering an improved overall transfer coefficient. J. Pet. Sci. Eng. 154, 479–487.
Jahanbakhsh, A., Liu, Q., Hadi Mosleh, M., Agrawal, H., Farooqui, N.M., Buckman, J., Recasens, M., Maroto-Valer, M., Korre, A., Durucan, S., 2021. An Investigation into CO_2–Brine–Cement–Reservoir Rock Interactions for Wellbore Integrity in CO_2 Geological Storage. Energies 14, 5033.
Kim, D., Oh, S., 2019. Relationship between the thermal properties and degree of saturation of cementitious grouts used in vertical borehole heat exchangers. Energy Build 201, 1–9.
Kim, Daehoon, Kim, G., Kim, Donghui, Baek, H., 2017. Experimental and numerical investigation of thermal properties of cement-based grouts used for vertical ground heat exchanger. Renew. energy 112, 260–267.
Kim, K.-H., Jeon, S.-E., Kim, J.-K., Yang, S., 2003. An experimental study on thermal conductivity of concrete. Cement and Concrete Research 33, 363–371.
Kiran, R., Teodoriu, C., Dadmohammadi, Y., Nygaard, R., Wood, D., Mokhtari, M., Salehi, S., 2017. Identification and evaluation of well integrity and causes of failure of well integrity barriers (A review). J. Nat. Gas Sci. Eng. 45, 511–526. https://doi.org/10.1016/j.jngse.2017.05.009.
Kulik, D.A., Winnefeld, F., Kulik, A., Miron, G.D., Lothenbach, B., 2021. CemGEMS–an easy-to-use web application for thermodynamic modelling of cementitious materials. RILEM Tech. Lett. 6, 36–52.
Lecampion, B., Bunger, A., Kear, J., Quesada, D., 2013. Interface debonding driven by fluid injection in a cased and cemented wellbore: Modeling and experiments. Int. J. Greenh. Gas Control 18, 208–223. https://doi.org/10.1016/j.ijggc.2013.07.012.
Lecampion, B., Quesada, D., Loizzo, M., Bunger, A., Kear, J., Deremble, L., Desroches, J., 2011. Interface debonding as a controlling mechanism for loss of well integrity: Importance for CO_2 injector wells. Energy Procedia 4, 5219–5226. https://doi.org/10.1016/j.egypro.2011.02.500.
Lemmon, E.W., Bell, I.H., Huber, M.L., McLinden, M.O., 2021. REFPROP: Reference Fluid Thermodynamic and Transport Properties. NIST Standard Reference Database 23. Version 10.0, 2018.
Linda, A., Singh, H.P., 2021. Geological Carbon Capture and Storage as a Climate-Change Mitigation Technology, in: Advances in Carbon Capture and Utilization. Springer, pp. 33–55.
Lindeberg, E., 2011. Modelling pressure and temperature profile in a CO_2 injection well. Energy Procedia 4, 3935–3941.
Log, T., Gustafsson, S.E., 1995. Transient plane source (TPS) technique for measuring thermal transport properties of building materials. Fire Mater 19, 43–49.
Loiseau, A., 2014. Thermal expansion of cement and well integrity of heavy oil wells. In: SPE Heavy and Extra Heavy Oil Conference: Latin America, Medellin, Colombia, September 2014. https://doi.org/10.2118/171066-MS.
Lothenbach, B., Matschei, T., Möschner, G., Glasser, F.P., 2008. Thermodynamic modelling of the effect of temperature on the hydration and porosity of Portland cement. Cem. Concr. Res. 38, 1–18.
Mathias, S.A., Gluyas, J.G., Oldenburg, C.M., Tsang, C.-F., 2010. Analytical solution for Joule–Thomson cooling during CO_2 geo-sequestration in depleted oil and gas reservoirs. Int. J. Greenh. Gas Control 4, 806–810.
Matschei, T., Lothenbach, B., Glasser, F.P., 2007. Thermodynamic properties of Portland cement hydrates in the system $CaO–Al_2O$ 3–SiO_2–$CaSO_4$–$CaCO_3$–H_2O. Cem. Concr. Res. 37, 1379–1410.
McCollom, T., 2011. Carbon Dioxide BT - Encyclopedia of Astrobiology, in: Gargaud, M., Amils, R., Quintanilla, J.C., Cleaves, H.J. (Jim), Irvine, W.M., Pinti, D.L., Viso, M. (Eds.). Springer Berlin Heidelberg, Berlin, Heidelberg, pp. 239–240. doi:10.1007/978-3-642-11274-4_1737.
Meyers, S.L., 1951. Thermal expansion characteristics of hardened cement paste and of concrete. In: Highway Research Board Proceedings 30, 193–203.
Mikunda, T., Brunner, L., Skylogianni, E., Monteiro, J., Rycroft, L., Kemper, J., 2021. Carbon capture and storage and the sustainable development goals. Int. J. Greenh. Gas Control 108, 103318.
Mitchell, L.J., 1953. Thermal expansion tests on aggregates, neat Cements, and concretes. American Society for Testing Materials, Proceedings 53, 963–975.
Mnahoncakova, E., Tesarek, P., Padevet, P., Cerny, R., 2006. Własności kompozytów cementowych wzmacnianych włóknem szklanym po poddaniu ich obciążeniu termicznemu. Cem. Wapno Bet. 11, 217–225.
Moghadam, A., Castelein, K., ter Heege, J., Orlic, B., 2021. A study on the hydraulic aperture of microannuli at the casing–cement interface using a large-scale laboratory setup. Geomech. Energy Environ., 100269
Moradi, B., Ayoub, M., Bataee, M., Mohammadian, E., 2020. Calculation of temperature profile in injection wells. J. Pet. Explor. Prod. Technol. 10, 687–697.
Nelson, E.B., Guillot, D. (Eds.), 2006. Well cementing, Second Edi. Schlumberger, Sugar Land, TXUSA, 77478.
Nelson, E.B., Michaux, M., 2006. Chemistry and characterization of Portland cement. In: Nelson, E.B., Guillot, D. (Eds.), Well Cementing. Schlumberger. Sugar Land, TXUSA, p. 773, 77478.
Nygaard, R., Salehi, S., Weideman, B., Lavoie, R.G., 2014. Effect of dynamic loading on wellbore leakage for the wabamun area CO_2-sequestration project. J. Can. Pet. Technol. 53, 69–82.
Oldenburg, C.M., 2007. Joule-Thomson cooling due to CO_2 injection into natural gas reservoirs. Energy Convers. Manag. 48, 1808–1815.
Orlic, B., 2009. Some geomechanical aspects of geological CO_2 sequestration. KSCE J. Civ. Eng. 13, 225–232. https://doi.org/10.1007/s12205-009-0225-2.
Powers, T.C., 1958. Structure and physical properties of hardened Portland cement paste. J. Am. Ceram. Soc. 41, 1–6.
Procesi, M., Cantucci, B., Buttinelli, M., Armezzani, G., Quattrocchi, F., Boschi, E., 2013. Strategic use of the underground in an energy mix plan: Synergies among CO_2, CH_4 geological storage and geothermal energy. Latium Region case study (Central Italy). Appl. Energy 110, 104–131. https://doi.org/10.1016/j.apenergy.2013.03.071.
Qomi, M.J.A., Ulm, F.-J., Pellenq, R.J.-M., 2015. Physical origins of thermal properties of cement paste. Phys. Rev. Appl. 3, 64010.
Reddy, B.R., Zhang, J., Ellis, M., 2016. Cement strength retrogression issues in offshore deep water applications - Do we know enough for safe cementing?. In: Offshore Technology Conference, Houston, Texas, USA, May 2016 https://doi.org/10.4043/27012-MS.
Ringrose, P., 2020. How to store CO_2 underground: Insights from early-mover CCS Projects. Springer.
Roy, P., Morris, J.P., Walsh, S.D.C., Iyer, J., Carroll, S., 2018. Effect of thermal stress on wellbore integrity during CO_2 injection. Int. J. Greenh. Gas Control 77, 14–26.
Roy, P., Walsh, S.D.C., Morris, J.P., Iyer, J., Hao, Y., Carroll, S., Gawel, K., Todorovic, J., Torsæter, M., 2016. Studying the impact of thermal cycling on wellbore integrity during CO_2 injection. In: 50th US Rock Mechanics/Geomechanics Symposium. OnePetro.
Sabri, S., Illston, J.M., 1982. Immediate and delayed thermal expansion of hardened cement paste. Cem. Concr. Res. 12, 199–208.
Samuel, R.J., Mahgerefteh, H., 2019. Investigating the impact of flow rate ramp-up on carbon dioxide start-up injection. Int. J. Greenh. Gas Control 88, 482–490.
Sanchez Fernandez, E., Naylor, M., Lucquiaud, M., Wetenhall, B., Aghajani, H., Race, J., Chalmers, H., 2016. Impacts of geological store uncertainties on the design and operation of flexible CCS offshore pipeline infrastructure. Int. J. Greenh. Gas Control 52, 139–154.
Santoyo, E., García, A., Morales, J.M., Contreras, E., Espinosa-Paredes, G., 2001. Effective thermal conductivity of Mexican geothermal cementing systems in the temperature range from 28°C to 200°C. Appl. Therm. Eng. 21, 1799–1812.
Sarkar, P.K., Mitra, N., 2021. Thermal conductivity of cement paste: Influence of macro-porosity. Cem. Concr. Res. 143, 106385.
Schimmel, M., Liu, W., Worrell, E., 2019. Facilitating sustainable geo-resources exploitation: A review of environmental and geological risks of fluid injection into hydrocarbon reservoirs. Earth-Sci. Rev. 194, 455–471.
Sellevold, E.J., Bjøntegaard, Ø., 2006. Coefficient of thermal expansion of cement paste and concrete: Mechanisms of moisture interaction. Mater. Struct. 39, 809–815.
Shui, Z., Zhang, R., Chen, W., Xuan, D., 2010. Effects of mineral admixtures on the thermal expansion properties of hardened cement paste. Constr. Build. Mater. 24, 1761–1767.
Skempton, A.W., 1954. The pore-pressure coefficients A and B. Geotechnique 4, 143–147.
Song, X., Zheng, R., Li, R., Li, G., Sun, B., Shi, Y., Wang, G., Zhou, S., 2019. Study on thermal conductivity of cement with thermal conductive materials in geothermal well. Geothermics 81, 1–11.
Szulczewski, M.L., MacMinn, C.W., Herzog, H.J., Juanes, R., 2012. Lifetime of carbon capture and storage as a climate-change mitigation technology. Proc. Natl. Acad. Sci 109, 5185–5189.
Taylor, H.F.W., 1992. Cement chemistry. Academic Press Limited, London, UK.
ter Heege, J.H., Orlic, B., Hoedeman, G.C., 2015. Characteristics of mechanical wellbore failure and damage: Insights of discrete element modelling and application to CO_2 storage. ARMA 15–174.
Thiercelin, M., Dargaud, B., Baret, J.F., Rodriquez, W.J., 1997. Cement design based on cement mechanical response. SPE Annu. Tech. 266–273.
Valenza II, J.J., Scherer, G.W., 2005. Evidence of anomalous thermal expansion of water in cement paste. Cem. Concr. Res. 35, 57–66.
Vrålstad, T., Skorpa, R., Opedal, N., De Andrade, J., 2015. Effect of thermal cycling on cement sheath integrity: realistic experimental tests and simulation of resulting leakages. In: SPE Thermal Well Integrity and Design Symposium. OnePetro.
Wadsö, L., Karlsson, J., Tammo, K., 2012. Thermal properties of concrete with various aggregates. Manuscript draft submitted to Cem. Concr. Res.
Wang, S., Jian, L., Shu, Z., Chen, S., Chen, L., 2020. A high thermal conductivity cement for geothermal exploitation application. Nat. Resour. Res. 29, 3675–3687.
Wise, J., Cedola, A., Nygaard, R., Hareland, G., Arild, Ø., Lohne, H.P., Ford, E.P., 2020. Wellbore Characteristics that Control Debonding Initiation and Microannuli Width in Finite Element Simulations. J. Pet. Sci. Eng. 191, 107157 https://doi.org/10.1016/j.petrol.2020.107157.
Wittmann, F., Lukas, J., 1974. Experimental study of thermal expansion of hardened cement paste. Mater. Constr. 7, 247–252.
Wolterbeek, T.K.T., Cornelissen, E.K., Hangx, S.J.T., Spiers, C.J., 2021a. Impact of downhole pressure and fluid-access on the effectiveness of wellbore cement expansion additives. Cem. Concr. Res. 147, 106514.

Wolterbeek, T.K.T., Cornelissen, E.K., Nolan, S., Todea, F., Stam, W., Roggeband, S.M., Dam, L., van Riet, E.J., Ruckert, F., Keultjes, W.J.G., 2021b. Restoration of annular zonal isolation using localized casing expansion (LCE) technology: A proof of concept based on laboratory studies and field trial results. J. Pet. Sci. Eng. 197, 108103 https://doi.org/10.1016/j.petrol.2020.108103.

Wolterbeek, T.K.T., Hangx, S.J.T., Spiers, C.J., 2016a. Effect of CO_2-induced reactions on the mechanical behaviour of fractured wellbore cement. Geomech. Energy Environ. 7, 26–46. https://doi.org/10.1016/j.gete.2016.02.002.

Wolterbeek, T.K.T., Peach, C.J., Raoof, A., Spiers, C.J., 2016b. Reactive transport of CO_2-rich fluids in simulated wellbore interfaces: Flow-through experiments on the 1-6 m length scale. Int. J. Greenh. Gas Control 54, 96–116. https://doi.org/10.1016/j.ijggc.2016.08.034.

Wolterbeek, T.K.T., Peach, C.J., Spiers, C.J., 2013. Reaction and transport in wellbore interfaces under CO_2 storage conditions: Experiments simulating debonded cement–casing interfaces. Int. J. Greenh. Gas Control 19, 519–529. https://doi.org/10.1016/j.ijggc.2013.10.017.

Wolterbeek, T.K.T., Raoof, A., 2018. Meter-Scale Reactive Transport Modeling of CO_2-Rich Fluid Flow along Debonded Wellbore Casing-Cement Interfaces. Environ. Sci. Technol. 52, 3786–3795. https://doi.org/10.1021/acs.est.7b05358.

Wolterbeek, T.K.T., Ruckert, F., van Moorsel, S.G., Cornelissen, E.K., 2019. Reactive transport and permeability evolution in wellbore defects exposed to periodic pulses of CO_2-rich water. Int. J. Greenh. Gas Control 91, 102835. https://doi.org/10.1016/j.ijggc.2019.102835.

Xu, Y., Chung, D.D.L., 2000a. Cement of high specific heat and high thermal conductivity, obtained by using silane and silica fume as admixtures. Cem. Concr. Res. 30, 1175–1178.

Xu, Y., Chung, D.D.L., 2000b. Effect of sand addition on the specific heat and thermal conductivity of cement. Cem. Concr. Res. 30, 59–61.

Yoon, S., Macphee, D.E., Imabi, M.S., 2014. Estimation of the thermal properties of hardened cement paste on the basis of guarded heat flow meter measurements. Thermochim. Acta 588, 1–10.

Zhang, M., Bachu, S., 2011. Review of integrity of existing wells in relation to CO_2 geological storage: What do we know? Int. J. Greenh. Gas Control 5, 826–840. https://doi.org/10.1016/j.ijggc.2010.11.006.

Zhu, J., 2019. Prevent Strength Retrogression Under Ultra High Temperature. In: Abu Dhabi International Petroleum Exhibition & Conference, Abu Dhabi, UAE, November 2019. https://doi.org/10.2118/197739-MS.